INTERNATIONAL JOURNAL FOR NUMERICAL METHODS IN ENGINEERING
Int. J. Numer. Meth. Engng 2009; **80**:815–845
Published online 23 February 2009 in Wiley InterScience (www.interscience.wiley.com). DOI: 10.1002/nme.2573

On impinging near-field granular jets

D. Arbelaez*, †, T. I. Zohdi and D. A. Dornfeld

Department of Mechanical Engineering, University of California, Berkeley, CA 94720-1740, U.S.A.

SUMMARY

In this work a multibody collision model, amenable to large-scale computation, is developed to simulate a jet of near-field grains impinging on a surface. This model is developed by computing momentum exchange for grain–grain and grain–surface interactions. The grain–grain interactions consist of collisions as well as near-field interactions. The analysis of these flows is separated into three components: (1) volume averaged quantities; (2) average surface tractions; and (3) average outflow conditions. For the surface stress calculations, parametric studies are performed on the properties of the surface and the grains through their coefficients of restitution, the strength of the near-field interactions, and the angle of attack of the jet. For the outflow calculations the flux of momentum through the simulation space is performed for varying near-field forces between the grains and varying degrees of surface roughness. Copyright © 2009 John Wiley & Sons, Ltd.

Received 30 June 2008; Revised 8 January 2009; Accepted 9 January 2009

KEY WORDS: granular flows; near-field effects; impinging jets

1. INTRODUCTION

There are many applications where granular materials strike a surface, for example manufacturing processes such as abrasive machining, fluid jet polishing, blast cleaning, and shot peening. Recently, several micro- and nanotechnology applications have emerged where the effects of near-field interaction between near-field grains and momentum exchange through mechanical contact must be taken into account in the analysis of these flows. For example, for many materials, relatively large electrostatic charges can build up for grains below the one millimeter scale. For general overviews of different granular physical phenomena, we refer the reader to work by Behringer and collaborators [1–3], Hutter and collaborators [4–17], and Jaeger and collaborators [18–26].

*Correspondence to: D. Arbelaez, Department of Mechanical Engineering, University of California, Berkeley, CA 94720-1740, U.S.A.
†E-mail: darbelae@me.berkeley.edu

Contract/grant sponsor: National Science Foundation; contract/grant number: DMI-20062085
Contract/grant sponsor: Alfred P. Sloan Foundation Minority PhD Program

In [26], Cheng *et al.* deal specifically with granular jets impinging on a surface. In this work, they demonstrate the similar physical behavior between a densely packed granular jet and a zero-surface tension fluid through experiments. Recently, Zohdi [27–30] has dealt with the computational aspects of granular flows including agglomeration in thermo-chemically reacting media, charge-induced clustering, and particle–fluid systems. In this work, we adapt aspects of these algorithms and develop analysis techniques to simulate a jet of near-field grains striking a surface that includes the following interactions: grain–grain and grain–surface collisions and grain–grain near-field forces. Specifically, these methods are extended to include rotation of the spherical grains, grain–surface collisions, and time-step size adaptivity to ensure that all possible grain–grain and grain–surface collisions are detected.

In this work, the analysis of these flows is divided into three parts: (1) volume averaged quantities; (2) average surface stresses; and (3) average outflow conditions. For the first part, desired quantities such as the density or velocity of the flow are computed by averaging over volumes in 'snap-shots' on a grid over time. For the second part, the examples focus on fairly dense granular flows, where the interaction between grains approaching the surface and those rebounding from the surface is significant. For these cases, the interactions between the grains affect the stress profile on the surface substantially. Previous research has been conducted on interference effects in non near-field particle streams. In [31–33], Ciampini, Papini, and collaborators develop and use an event-driven MD simulation to study the effect of interference between incoming and rebounding particles on the available power transferred to the surface. Owing to the event-driven nature of the simulation, near-field forces cannot be considered using their algorithm. In this work, a different analysis method is also presented, where the average stress is computed over the entire surface to obtain a surface stress profile. Finally, for the third part of the analysis, the flux of desired quantities across the interface of a control volume is measured.[‡] For the surface stress calculations, two- and three-dimensional examples are presented. For the outflow calculations, statistical moments of the flux profiles are defined and sample two-dimensional calculations are presented.

2. SYSTEM CONFIGURATION

In this section, an algorithm is developed to model the particulate flow coming from a source, striking a surface, and moving outside of the region of interest. Figure 1 shows a schematic of the simulation, here the source is the inflow region, where the grains are introduced, and the region of interest is bounded by the outflow region, where the grains are removed from the simulation. Initially, spherical grains[§] are placed at random positions in the inflow region for the given volume fraction, and they are prescribed velocities that match a given velocity profile. The introduction of new grains is performed subject to the constraint that the volume fraction of grains in the inflow region remains constant over time. In order to meet this constraint, a new grain is introduced in the inflow region whenever another grain leaves this region. Specifically, it is introduced at the top of the box in a random spot along the $\mathbf{e}_1'$ direction. The grains are introduced at the top of the

[‡] In this work, the terms fluxes across the interface and outflow calculations are used interchangeably.

[§] There are many applications where the grains are not exactly spherical, but are close enough to be approximated as such for this analysis.

DOI: 10.1002/nme

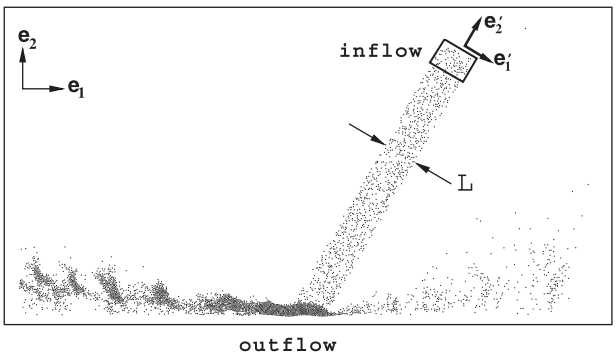

Figure 1. Schematic of the granular jet simulation. The grains are introduced in the inflow region and removed at the outflow region.

box so that the volume fraction remains fixed until the grains start interacting with one another near the surface. Whenever a grain leaves the outflow box it is removed from the simulation.

3. MATHEMATICAL FORMULATION

In this model the following interactions are considered: grain–grain near-field interactions, grain–grain collisions, and grain–surface collisions. Once these interactions are modeled the position of each grain is found from the equations of motion

$$\begin{aligned} m_i \ddot{\mathbf{r}}_i &= \boldsymbol{\Psi}_i^{\mathrm{nf}} + \boldsymbol{\Psi}_i^{\mathrm{c}} + \boldsymbol{\Psi}_i^{\mathrm{f}} \\ I_i \dot{\boldsymbol{\omega}}_i &= \mathbf{M}_i^{\mathrm{f}} \end{aligned} \tag{1}$$

where m_i and I_i are the mass and moment of inertia of grain i, respectively; $\mathbf{r}_i$ is the position of the centroid of grain i, $\boldsymbol{\omega}_i$ is the angular velocity of grain i, $\boldsymbol{\Psi}_i^{\mathrm{nf}}$ is the near-field force, $\boldsymbol{\Psi}_i^{\mathrm{c}}$ is the contact force, $\boldsymbol{\Psi}_i^{\mathrm{f}}$ is the friction force, and $\mathbf{M}^{\mathrm{f}}$ is the total moment due to friction acting on grain i. Note that in this work the grains are always assumed to be spherical.

In [27], Zohdi introduced a model for the impact between grains under the influence of near field and other external forces. This model is used to determine the normal and frictional forces for grain–grain collisions. In this work, this model is extended to include the effect of the rotation of the grains on the frictional forces during the grain–grain collisions. All of the equations derived in [27] are reformulated with this in mind. Another improvement on the model introduced in [27] is the inclusion in this work of grain–surface collisions with normal and frictional forces. As with the grain–grain collisions, the grain–surface interactions include rotational effects. In Section 6 a measure of the average stress on the surface is introduced. The inclusion of rotational effects during the grain–surface collisions is critical to accurately resolve the average shear stress on the surface. The simplest example of this is a rotating grain approaching a surface in the surface normal direction. If rotational effects were not included in the friction force, a significant error could be made in this calculation. In the following subsections the models for each individual interaction will be presented.

DOI: 10.1002/nme

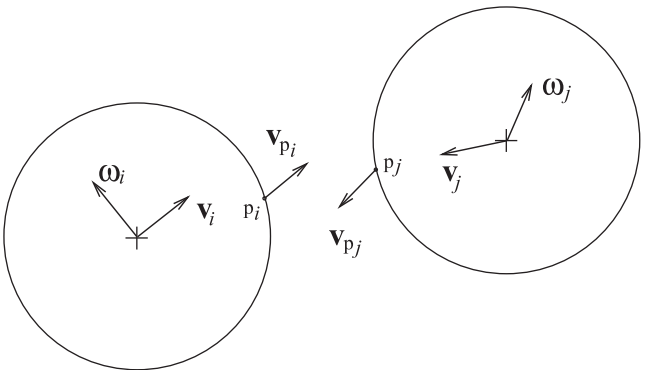

Figure 2. Schematic of grains i and j with velocities $\mathbf{v}_i$ and $\mathbf{v}_j$ and angular velocities $\boldsymbol{\omega}_i$ and $\boldsymbol{\omega}_j$ approaching each other.

3.1. Grain–grain interaction

The grain–grain interaction consists of near-field forces and contact and frictional forces at the contact point on each grain. This is equivalent to a force and a moment acting on the center of each grain. Consider the two spheres with mass m_i and m_j, which are shown in Figure 2, their motion is described by their centroid velocities $\mathbf{v}_i$ and $\mathbf{v}_j$ and their angular velocities $\boldsymbol{\omega}_i$ and $\boldsymbol{\omega}_j$ as they approach each other. Assuming that the spheres do not deform, they will come in contact at point p_i on sphere i and at point p_j on sphere j. The velocity of grain i at point p_i is given by $\mathbf{v}_{pi}=\mathbf{v}_i+\boldsymbol{\omega}_i\times(r_i\mathbf{n}_{ij})$, whereas the velocity of grain j at point p_j is given by $\mathbf{v}_{pj}=\mathbf{v}_j-\boldsymbol{\omega}_j\times(r_j\mathbf{n}_{ij})$, where $\mathbf{n}_{ij}=(\mathbf{r}_j-\mathbf{r}_i)/\|\mathbf{r}_j-\mathbf{r}_i\|$ is a unit vector pointing from the center of grain i to the center of grain j, $\mathbf{r}_i$ and $\mathbf{r}_j$ are the positions of the centroids of grains i and j, respectively; and r_i and r_j are the radii of grains i and j, respectively. The relative velocity between the point p_i on sphere i and at point p_j on sphere j is given by $\mathbf{v}_{\text{rel}}=\mathbf{v}_{pj}-\mathbf{v}_{pi}$. The vector $\mathbf{v}_{\text{rel}}$ can be decomposed into normal and tangential components $\mathbf{v}_{\text{rel}}=v^n_{\text{rel}}\mathbf{n}_{ij}+v^t_{\text{rel}}\mathbf{t}$, where $\mathbf{t}$ is given by

$$\mathbf{t}=\frac{\mathbf{v}_{\text{rel}}-(\mathbf{n}_{ij}\cdot\mathbf{v}_{\text{rel}})\mathbf{n}_{ij}}{\|\mathbf{v}_{\text{rel}}-(\mathbf{n}_{ij}\cdot\mathbf{v}_{\text{rel}})\mathbf{n}_{ij}\|} \tag{2}$$

An orthonormal basis can now be defined by the vectors $(\mathbf{n}_{ij},\mathbf{t},\mathbf{s})$, where the transverse unit vector is given by $\mathbf{s}=\mathbf{n}_{ij}\times\mathbf{t}$. When these grains come into contact, the force on grain i is given by $\mathbf{f}_i=-f_c\mathbf{n}_{ij}+f_f\mathbf{t}$, the force on grain j is given by $\mathbf{f}_j=f_c\mathbf{n}_{ij}-f_f\mathbf{t}$, the moment on grain i is given by $\mathbf{M}_i=(r_i f_f)\mathbf{s}$, and the moment on grain j is given by $\mathbf{M}_j=(r_j f_f)\mathbf{s}$, where $f_c\geqslant 0$ and $f_f\geqslant 0$.

3.1.1. Near-field interaction. In this work the near-field interaction is modeled by a general central-force attraction–repulsion form given by

$$\boldsymbol{\Psi}^{\text{nf}}_i=\sum_{j\neq i}^{N_p}(\alpha_1\|\mathbf{r}_i-\mathbf{r}_j\|^{-\beta_1}-\alpha_2\|\mathbf{r}_i-\mathbf{r}_j\|^{-\beta_2})\mathbf{n}_{ij} \tag{3}$$

DOI: 10.1002/nme

where α_1, α_2, β_1, and β_2 are nonnegative parameters. The general form given in Equation (3) represents different types of physical phenomena, for given values of the parameters α_1, α_2, β_1, and β_2 .

3.1.2. Normal contact interaction. The contact interaction between the grains is computed through a balance of linear momentum in the normal direction. The balance of linear momentum, in the direction $\mathbf{n}_{ij}$, for a grain i is given by

$$m_i v_{in}(t) - \delta t \overline{f}_c + \int_t^{t+\delta t} E_{in}\,\mathrm{d}t = m_i v_{in}(t+\delta t) \tag{4}$$

where t corresponds to the time immediately before the grains come into contact, δt is the impact duration time, $t+\delta t$ corresponds to the time immediately after the collision occurs, $\delta t \overline{f}_c = \int_t^{t+\delta t} f_c\,\mathrm{d}t$, and $E_{in} = \mathbf{E}_i \cdot \mathbf{n}_{ij}$, where $\mathbf{E}_i$ is the sum of external forces acting on grain i. In this case $\overline{f}_c$ is interpreted to be the average normal impulsive force. Similarly, for grain j, the balance of linear momentum in the normal contact direction gives

$$m_j v_{jn}(t) + \delta t \overline{f}_c + \int_t^{t+\delta t} E_{jn}\,\mathrm{d}t = m_j v_{jn}(t+\delta t) \tag{5}$$

where $E_{jn} = \mathbf{E}_j \cdot \mathbf{n}_{ij}$ and $\mathbf{E}_j$ is the sum of external forces acting on grain j. In order to solve for the velocities after impact, an estimate for the coefficient of restitution, e, must be provided. The coefficient of restitution is defined as

$$e = \frac{\int_{t+\delta t_1}^{t+\delta t} f_c\,\mathrm{d}t}{\int_t^{t+\delta t_1} f_c\,\mathrm{d}t} \tag{6}$$

which is the ratio of the impulse during the recovery phase, occurring in the time interval $(t+\delta t_1, t+\delta t)$, to the impulse during the compression phase, occurring in the time interval $(t, t+\delta t_1)$. The balance of momentum for both grains can also be divided into a compression phase and a recovery phase. For the compression phase the balance of momentum for grains i and j in the normal direction is

$$\begin{aligned} m_i v_{in}(t) - \int_t^{t+\delta t_1} f_c\,\mathrm{d}t + \int_t^{t+\delta t_1} E_{in}\,\mathrm{d}t &= m_i v_{cn} \\ m_j v_{jn}(t) + \int_t^{t+\delta t_1} f_c\,\mathrm{d}t + \int_t^{t+\delta t_1} E_{jn}\,\mathrm{d}t &= m_j v_{cn} \end{aligned} \tag{7}$$

where v_{cn} is a common velocity for both grains since their relative velocity in the normal direction vanishes at time $t+\delta t_1$. Similarly, for the recovery phase, the balance of momentum for grains i and j in the normal direction is

$$\begin{aligned} m_i v_{cn} - \int_{t+\delta t_1}^{t+\delta t} f_c\,\mathrm{d}t + \int_{t+\delta t_1}^{t+\delta t} E_{in}\,\mathrm{d}t &= m_i v_{in}(t+\delta t) \\ m_j v_{cn} + \int_{t+\delta t_1}^{t+\delta t} f_c\,\mathrm{d}t + \int_{t+\delta t_1}^{t+\delta t} E_{jn}\,\mathrm{d}t &= m_j v_{jn}(t+\delta t) \end{aligned} \tag{8}$$

DOI: 10.1002/nme

Using Equations (6)–(8), the coefficient of restitution can be written as

$$e=\frac{v_{jn}(t+\delta t)-v_{in}(t+\delta t)+1/m_i\ \int_{t+\delta t_1}^{t+\delta t}E_{in}\,\mathrm{d}t-1/m_j\int_{t+\delta t_1}^{t+\delta t}E_{jn}\,\mathrm{d}t}{v_{in}(t)-v_{jn}(t)+1/m_i\int_t^{t+\delta t_1}E_{in}\,\mathrm{d}t-1/m_j\int_t^{t+\delta t_1}E_{jn}\,\mathrm{d}t} \tag{9}$$

Using Equations (4), (5), and (9) the normal impulse is given by

$$\overline{f}_c\delta t=\frac{(1+e)m_im_j}{m_i+m_j}\left[v_{in}(t)-v_{jn}(t)+\frac{1}{m_i}\int_t^{t+\delta t_1}E_{in}\,\mathrm{d}t-\frac{1}{m_j}\int_t^{t+\delta t_1}E_{jn}\,\mathrm{d}t\right] \tag{10}$$

In order to use Equation (10), estimates must be provided for the coefficient of restitution and the impact time. For extensive experimental data on the coefficient of restitution see Goldsmith [34]. The impact time can be estimated using solutions for linear elastic bodies, for example, see the work by Johnson [35] for details. As an approximation, Equation (4) can be discretized in time, with time step Δt, giving the following equation as:

$$m_iv_{in}(t)-\overline{f}_c\delta t+\overline{E}_{in}\delta t\approx m_iv_{in}(t+\Delta t) \tag{11}$$

where $\delta t\ll\Delta t$ and $\overline{E}_{in}\delta t=\int_t^{t+\delta t}E_{in}\,\mathrm{d}t$. Equation (11) can now be rewritten as

$$m_i\frac{v_{in}(t+\Delta t)-v_{in}(t)}{\Delta t}\approx-\frac{\overline{f}_c\delta t}{\Delta t}+\frac{\overline{E}_{in}\delta t}{\Delta t} \tag{12}$$

noting that $m_i(v_{in}(t+\Delta t)-v_{in}(t))/\Delta t$ is a difference formula for $m_i\dot{v}_{in}$, then the normal contact contribution of grain–grain interaction force can be defined as

$$\mathbf{\Psi}_i^{\mathrm{c}}=-\frac{\overline{f}_c\delta t}{\Delta t}\mathbf{n}_{ij} \tag{13}$$

3.1.3. Frictional interaction. The friction force between the grains is computed through a balance of linear momentum in the tangential direction, and a balance of angular momentum in the transverse direction for grains i and j. The balance of linear momentum, in the tangential direction, for grain i is given by

$$m_iv_{it}(t)+\delta t\overline{f}_f+\int_t^{t+\delta t}E_{it}\,\mathrm{d}t=m_iv_{it}(t+\delta t) \tag{14}$$

where $\delta t\overline{f}_f=\int_t^{t+\delta t}f_f\,\mathrm{d}t$, so that in this case $\overline{f}_f$ is interpreted to be the average friction force for the grain–grain collision, and $E_{it}=\mathbf{E}_i\cdot\mathbf{t}$. For grain j the balance of linear momentum in the tangential direction is

$$m_jv_{jt}(t)-\delta t\overline{f}_f+\int_t^{t+\delta t}E_{jt}\,\mathrm{d}t=m_jv_{jt}(t+\delta t) \tag{15}$$

where $E_{jt}=\mathbf{E}_j\cdot\mathbf{t}$. The balance of angular momentum, in the transverse direction, for grain i is given by

$$I_i\omega_{is}(t)+r_i\overline{f}_f\delta t+\int_t^{t+\delta t}M_{is}\,\mathrm{d}t=I_i\omega_{is}(t+\delta t) \tag{16}$$

DOI: 10.1002/nme

where $r_i \overline{f}_f \delta t = \int_t^{t+\delta t} (r_i \mathbf{n}_{ij}) \times \mathbf{f}_i \cdot \mathbf{s} \, \mathrm{d}t$ is the moment of impulse, and $M_{is} = \mathbf{M}_i \cdot \mathbf{s}$ is the sum of external moments on grain i in the transverse direction. Similarly, the balance of angular momentum, in the transverse direction, for grain j is given by

$$I_j \omega_{js}(t) + r_j \overline{f}_f \delta t + \int_t^{t+\delta t} M_{js} \, \mathrm{d}t = I_j \omega_{js}(t+\delta t) \tag{17}$$

where $M_{js} = \mathbf{M}_j \cdot \mathbf{s}$ is the sum of external moments on grain j in the transverse direction.

For the frictional interaction, a Coulomb friction stick–slip model is used, where during contact the grain will stick at the contact point if $f_f \leqslant \mu_s f_c$, where μ_s is the static coefficient of friction, and the grain will slip otherwise. In order to determine the friction force, the assumption that the grains stick is first adopted. Therefore, $v_{\mathrm{rel}}^t = 0$, which leads to the following kinematic relation at time $t+\delta t$

$$v_{jt}(t+\delta t) - r_j \omega_{js}(t+\delta t) = v_{it}(t+\delta t) + r_i \omega_{is}(t+\delta t) \tag{18}$$

Using Equations (14)–(18) and $I_i = \frac{2}{5} m_i r_i^2$ for a sphere, the tangential impulse is given by

$$\overline{f}_f \delta t = \frac{2}{7} \frac{m_i m_j}{m_i + m_j} \left\{ (v_{jt}(t) - r_j \omega_{js}(t)) - (v_{it}(t) + r_i \omega_{is}(t)) + \left[\frac{1}{m_j} \left(\overline{E}_{jt} - \frac{5}{2} \frac{\overline{M}_{js}}{r_j} \right) - \frac{1}{m_i} \left(\overline{E}_{it} + \frac{5}{2} \frac{\overline{M}_{is}}{r_i} \right) \right] \delta t \right\} \tag{19}$$

Now that the friction force has been determined with the sticking assumption, this assumption must be verified. If $f_f > \mu_s f_c$, then the sticking assumption does not hold and slip occurs. Using the Coulomb friction model, the friction force is $f_f = \mu_d f_c$, where μ_d is the dynamic coefficient of friction. In summary, the grain–grain frictional interaction, applied to the discretized equations, is given by

$$\mathbf{\Psi}_i^{\mathrm{f}} = \begin{cases} \dfrac{|\overline{f}_f| \delta t}{\Delta t} \mathbf{t} & \text{if } |\overline{f}_f| \leqslant \mu_s |\overline{f}_c| \\ \mu_d \| \mathbf{\Psi}_i^{\mathrm{c}} \| \mathbf{t} & \text{if } |\overline{f}_f| > \mu_s |\overline{f}_c| \end{cases} \tag{20}$$

3.2. Grain–surface interaction

The grain–surface interaction consists of contact and frictional forces at the contact point on the grain. This is equivalent to a force and a moment acting on the center of the grain. Consider the sphere with mass m, which is shown in Figure 3, its motion is described by its centroid velocity $\mathbf{v}$ and angular velocity $\boldsymbol{\omega}$ as it approaches a surface with normal $\mathbf{n}$. Assuming that the sphere does not deform, it will come in contact with the surface at point p. The velocity at this point is given by $\mathbf{v}_p = \mathbf{v} - \boldsymbol{\omega} \times (r\mathbf{n})$. The vector $\mathbf{v}_p$ can be decomposed into normal and tangential components $\mathbf{v}_p = v_n \mathbf{n} + v_t \mathbf{t}$, where $\mathbf{t}$ is given by

$$\mathbf{t} = \frac{\mathbf{v}_p - (\mathbf{n} \cdot \mathbf{v}_p)\mathbf{n}}{\| \mathbf{v}_p - (\mathbf{n} \cdot \mathbf{v}_p)\mathbf{n} \|} \tag{21}$$

DOI: 10.1002/nme

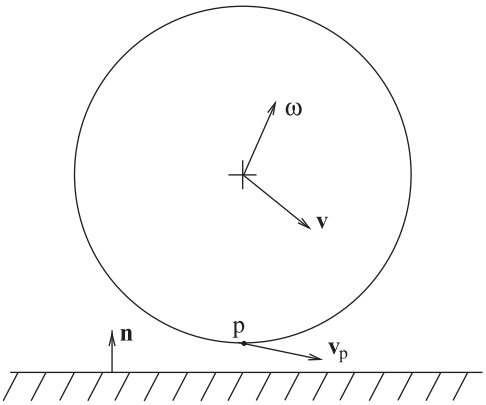

Figure 3. Schematic of a grain with velocity **v** and angular velocity **ω** approaching a surface with normal **n**.

An orthonormal basis can now be defined by the vectors $(\mathbf{n}, \mathbf{t}, \mathbf{s})$ where the transverse unit vector is given by $\mathbf{s}=\mathbf{n}\times\mathbf{t}$. Using these definitions the force on the grain is given by $\mathbf{f}=f_c\mathbf{n}-f_f\mathbf{t}$ and the moment on the grain is given by $\mathbf{M}=(rf_f)\mathbf{s}$, where $f_c \geqslant 0$ and $f_f \geqslant 0$.

3.2.1. Normal contact interaction. The contact force between the grain and the surface is computed through a balance of linear momentum in the normal direction. The balance of linear momentum, in the direction normal to the surface, for grain i is given by

$$m_i v_{in}(t)+\delta t\,\overline{f}_c+\int_t^{t+\delta t} E_{in}\,\mathrm{d}t = m_i v_{in}(t+\delta t) \tag{22}$$

where $\delta t\,\overline{f}_c=\int_t^{t+\delta t} f_c\,\mathrm{d}t$, so that in this case $\overline{f}_c$ is interpreted to be the average normal impulsive force exerted by the surface on the grain, and $E_{in}=\mathbf{E}_i\cdot\mathbf{n}$, where $\mathbf{E}_i$ is the sum of external forces acting on grain i. The compression phase for the grain occurs for the time interval $(t, t+\delta t_1)$, for this interval the balance of linear momentum in the normal direction of contact is given by

$$m_i v_{in}(t)+\int_t^{t+\delta t_1} f_c\,\mathrm{d}t+\int_t^{t+\delta t_1} E_{in}\,\mathrm{d}t = m_i v_{cn}=0 \tag{23}$$

where $v_{cn}=0$ since the relative velocity in the normal direction between the surface and the grain vanishes at time $t+\delta t_1$. For the recovery phase that occurs in the time interval $(t+\delta t_1, t+\delta t)$, the balance of linear momentum in the normal contact direction is given by

$$\int_{t+\delta t_1}^{t+\delta t} f_c\,\mathrm{d}t+\int_{t+\delta t_1}^{t+\delta t} E_{in}\,\mathrm{d}t = m_i v_{in}(t+\delta t) \tag{24}$$

DOI: 10.1002/nme

where on the left side of Equation (24) a momentum term does not appear since the velocity of the grain at time $t+\delta t_1$ vanishes. Using the definition given in Equation (6), the coefficient of restitution is

$$e = \frac{v_{in}(t+\delta t) - 1/m_i \int_{t+\delta t_1}^{t+\delta t} E_{in}\,\mathrm{d}t}{-v_{in}(t) - 1/m_i \int_{t}^{t+\delta t_1} E_{in}\,\mathrm{d}t} \tag{25}$$

Using Equations (22) and (25), the velocity of grain i in the normal direction after impact is the normal impulse is given by

$$\overline{f}_c \delta t = -(1+e)\left[m_i v_{in}(t) + \int_t^{t+\delta t} E_{in}\,\mathrm{d}t \right] \tag{26}$$

Similar to the interaction force for the grain–grain contact interaction given in the previous section, the grain–surface contact interaction applied after discretization is

$$\mathbf{\Psi}_i^{\mathrm{c}} = \frac{\overline{f}_c \delta t}{\Delta t}\mathbf{n} \tag{27}$$

3.2.2. Frictional interaction. The friction force between the grain and the surface is computed through a balance of linear momentum in the tangential direction, and a balance of angular momentum in the transverse direction. The balance of linear momentum, in the tangential direction, for grain i is given by

$$m_i v_{it}(t) + \delta t \overline{f}_f + \int_t^{t+\delta t} E_{it}\,\mathrm{d}t = m_i v_{it}(t+\delta t) \tag{28}$$

where $\delta t \overline{f}_f = \int_t^{t+\delta t} f_f\,\mathrm{d}t$, so that in this case $\overline{f}_f$ is interpreted to be the average friction force exerted by the surface on the grain, and $E_{it} = \mathbf{E}_i \cdot \mathbf{t}$. The balance of angular momentum, in the transverse direction, for grain i is given by

$$I_i \omega_{is}(t) + \delta t r_i \overline{f}_f + \int_t^{t+\delta t} M_{is}\,\mathrm{d}t = I_i \omega_{is}(t+\delta t) \tag{29}$$

where $\delta r_i t \overline{f}_f = \int_t^{t+\delta t} (-r_i \mathbf{n}) \times \mathbf{f} \cdot \mathbf{s}\,\mathrm{d}t$ is the moment of impulse exerted by the surface on the grain, and $M_{is} = \mathbf{M}_i \cdot \mathbf{s}$ is the sum of external moments in the transverse direction.

For the frictional interaction the same Coulomb friction stick–slip model that is used for the grain–grain interaction is employed. In order to determine the friction force, the assumption that the grain sticks is first adopted. Therefore $\mathbf{v}_p \cdot \mathbf{t} = 0$, which leads to the following kinematic relation at time $t+\delta t$:

$$v_{it}(t+\delta t) = r_i \omega_{is}(t+\delta t) \tag{30}$$

Using Equations (28)–(30) and $I_i = \frac{2}{5} m_i r_i^2$ for a sphere, the tangential impulse is given by

$$\overline{f}_f \delta t = \frac{2}{7}\left\{ m_i (v_{it}(t) - r_i \omega_{is}(t)) + \int_t^{t+\delta t} E_{it}\,\mathrm{d}t - \frac{5}{2r_i}\int_t^{t+\delta t} M_{is}\,\mathrm{d}t \right\} \tag{31}$$

DOI: 10.1002/nme

Now that the friction force has been determined with the sticking assumption, this assumption must be verified. If $f_f > \mu_s f_c$, then the sticking assumption does not hold and slip occurs. Using the Coulomb friction model, the friction force is $f_f = \mu_d f_c$, where μ_d is the dynamic coefficient of friction. In summary, the grain–surface frictional interaction, applied to the discretized equations, is given by

$$\boldsymbol{\Psi}_i^{\mathrm{f}} = \begin{cases} -\dfrac{|\overline{f}_f|\delta t}{\Delta t}\mathbf{t} & \text{if } |\overline{f}_f| \leqslant \mu_s |\overline{f}_c| \\ -\mu_d \|\boldsymbol{\Psi}_i^{\mathrm{c}}\|\mathbf{t} & \text{if } |\overline{f}_f| > \mu_s |\overline{f}_c| \end{cases} \tag{32}$$

4. TEMPORAL DISCRETIZATION AND ITERATIVE SOLUTION

In this work the set of ordinary differential equations is solved using the implicit Euler method. For the first-order system $\dot{y} = f$, the implicit Euler scheme is given by $y(t+\Delta t) = y(t) + \Delta t f(t+\Delta t)$. The discretization of Equation (1) is then given by

$$\begin{aligned} \mathbf{r}_i^{L+1} &= \frac{\Delta t^2}{m_i}\boldsymbol{\Psi}_i^{\mathrm{tot}}(\mathbf{r}_i^{L+1}) + \mathbf{r}_i^L + \Delta t \dot{\mathbf{r}}_i^L \\ \boldsymbol{\omega}_i^{L+1} &= \frac{\Delta t}{I_i}\mathbf{M}_i^{\mathrm{tot}} + \boldsymbol{\omega}_i^L \end{aligned} \tag{33}$$

where the superscripts L and $L+1$ correspond to the times t and $t+\Delta t$, respectively. Note that $\mathbf{M}_i^{\mathrm{tot}}$ corresponds the average moment exerted during a collision, which is taken to be constant during the impact; therefore, there is no L or $L+1$ superscript on $\mathbf{M}_i^{\mathrm{tot}}$. To solve Equation (33), an iterative scheme must be used. One possible solution scheme is Newton's method; however, the tangent matrix may not be easy to form due to the lack of smoothness of the trajectories of the grains. This lack of smoothness is produced by the impacts of grains with other grains or surfaces. Another option is to use a fixed point iteration that usually converges at a slower rate but is expected to be more robust. In order to solve Equation (33) with a fixed point iteration, it is written as

$$\mathbf{r}_i^{L+1,k+1} = \frac{\Delta t^2}{m_i}\boldsymbol{\Psi}_i^{\mathrm{tot}}(\mathbf{r}_i^{L+1,k}) + \mathbf{r}_i^L + \Delta t \dot{\mathbf{r}}_i^L \tag{34}$$

where k indicates the iteration count. In [27–30], Zohdi shows that the error at iteration k can be bounded by $\|e^k\| \leqslant \eta^k \|e^0\|$, where $\eta \propto \Delta t^2/m_i$. Therefore, the fixed point iteration is guaranteed to converge when $\eta < 1$, implying that the method converges as long as the time-step size is small enough. If convergence is slow within a time step, the time-step size can be reduced to increase the rate of convergence; however, it is desirable that the time-step sizes are maximized in order to reduce the computation time. By controlling the number of iterations needed for convergence, Zodhi [27–30] derives the following expression for time-step adaptivity:

$$\Delta t_{\mathrm{tol}} = \left(\frac{\left(\dfrac{\mathrm{Tol}}{e^0}\right)^{1/pk_d}}{\left(\dfrac{e^k}{e^0}\right)^{1/pk}} \right) \Delta t \tag{35}$$

DOI: 10.1002/nme

where Tol is the convergence tolerance, k_d is the desired number of iterations, and $p=2$ corresponds to the exponent on Δt in the expression $\eta \propto \Delta t^2/m_i$. When the solution does not converge in the desired number of iterations, Equation (35) can be used to compute a new time-step size from the previous time-step size used. If the solution does converge in less than k_d iterations, then the time-step size can be recomputed in order to achieve convergence in the desired number of iterations for the next time step. When this occurs the method computes a larger time-step size for the next time step. It is important that the time-step size does not increase above a point where collisions are missed or the truncation error becomes too large. For this reason, a maximum time-step size, $\Delta t^{\lim}$, is chosen to ensure that the physics of the process is not lost in the numerical discretization. At the implementation level, the smallest of the iteration-limited and collision-limited time-step sizes is chosen. In event-driven molecular dynamics, the simulation is moved forward as events occur (i.e. collisions). The reader is referred to [36] or [37] for a detailed description of these types of simulations. In order to move the time step forward, the time for the next collision is computed. In these types of simulations only collision interactions are considered; therefore, the collision times can be computed exactly. In this work, this is not possible since near field and other external forces are considered. However, as similar approach can be used to control the time-step size such that no collisions are missed in the simulation.

First, the collision time is calculated as it would be in an event-driven simulation, for this case near field and external forces are neglected. Consider two spheres i and j with radii r_i and r_j, respectively. The spheres collide when the following is satisfied:

$$\|\mathbf{r}_j(t_c)-\mathbf{r}_i(t_c)\|=r_i+r_j \tag{36}$$

where t_c corresponds to the time when the grains first come into contact. Since no forces are considered to act on the grains, the position of grain i at time t_c can be expressed as

$$\mathbf{r}_i(t_c)=\mathbf{r}_i(t)+(t_c-t)\dot{\mathbf{r}}_i(t) \tag{37}$$

where t is the current time. A similar expression can be written for grain j, and using Equations (36) and (37) produces a quadratic equation for t_c

$$\|\mathbf{r}_{ij}+(t_c-t)\dot{\mathbf{r}}_{ij}\|^2=(r_i+r_j)^2 \tag{38}$$

where $\mathbf{r}_{ij}=\mathbf{r}_j(t)-\mathbf{r}_i(t)$ and $\dot{\mathbf{r}}_{ij}=\dot{\mathbf{r}}_j(t)-\dot{\mathbf{r}}_i(t)$. Equation (38) is then solved to determine the collision time interval

$$t_c-t=\frac{(-\mathbf{r}_{ij}\cdot\dot{\mathbf{r}}_{ij})\pm\sqrt{\mathbf{\Gamma}_{ij}}}{\|\dot{\mathbf{r}}_{ij}\|^2} \tag{39}$$

where $\mathbf{\Gamma}_{ij}=(\mathbf{r}_{ij}\cdot\dot{\mathbf{r}}_{ij})^2-\|\dot{\mathbf{r}}_{ij}\|^2(\|\mathbf{r}_{ij}\|^2-(r_i+r_j)^2)$. Equation (39) represents the following three possible scenarios regarding the collision between grains i and j:

1. Either $\mathbf{r}_{ij}\cdot\dot{\mathbf{r}}_{ij}>0$ or $\mathbf{r}_{ij}\cdot\dot{\mathbf{r}}_{ij}<0$. If $\mathbf{r}_{ij}\cdot\dot{\mathbf{r}}_{ij}>0$ the grains are moving away from each other and a collision cannot occur; therefore, a collision is only possible if $\mathbf{r}_{ij}\cdot\dot{\mathbf{r}}_{ij}<0$.
2. Either $\mathbf{\Gamma}_{ij}<0$ or $\mathbf{\Gamma}_{ij}>0$. If $\mathbf{\Gamma}_{ij}<0$ the collision time is a complex number, this represents the case when grains do not collide. Therefore, if $\mathbf{\Gamma}_{ij}>0$ and $\mathbf{r}_{ij}\cdot\dot{\mathbf{r}}_{ij}<0$ then a collision will occur and Equation (39) can be used to compute the collision time.
3. If a collision occurs, Equation (39) has either one or two real roots. If there are two roots, the smaller time represents the actual collision time between the grains. The case where the solution to Equation (39) has only one real root corresponds to grazing contact.

DOI: 10.1002/nme

In the previous discussion, it was assumed that no external or near-field forces act on the grains. Since this is not the case, it is not possible to predict the collision time in such a simple manner. However, in this work it is not necessary to determine exact collision times, the goal is to adapt the time-step size in order to prevent interpenetration of grains. The time-step size should be chosen so that at any time two grains may only overlap by a small fraction of their radii. Therefore, at time t, the maximum time-step size should be the sum of the collision time interval, $\Delta t_c = t_c - t$, and the maximum allowable overlap between grains, $\gamma \min(r_i, r_j)/\|\dot{\mathbf{r}}_{ij}\|$. Since no external or near-field forces were considered in the calculation of the collision time interval, Δt_c is scaled by a factor $\eta < 1$.[¶] In summary, the limiting time-step size as determined by grain–grain collisions is

$$\Delta t_{ij}^{\lim} = \eta \Delta t_c + \frac{\gamma \min(r_i, r_j)}{\|\dot{\mathbf{r}}_{ij}\|} \tag{40}$$

where Δt_c is determined using Equation (39).

In a similar manner, the limiting time-step size for a grain–surface collision can also be calculated. In this case, the collision time interval for a grain–surface collision[‖] is

$$t_c - t = -\frac{\mathbf{d}_{ij} \cdot \mathbf{n}_j}{\dot{\mathbf{r}}_i \cdot \mathbf{n}_j} \tag{41}$$

where $\mathbf{d}_{ij}$ is a vector from any point on the surface of triangle j to the center of grain i, $\mathbf{n}_j$ is the normal to triangle j. Note that if $\dot{\mathbf{r}}_i \cdot \mathbf{n}_j > 0$, the grain is moving away from the surface and contact is impossible. In practice, the limiting time-step size chosen is the sum of maximum allowable overlap between the grain and the surface and a scaled factor of the collision time interval. The limiting time-step size as determined by grain–surface collisions is then

$$\Delta t_{ij}^{\lim} = \eta \Delta t_c + \frac{\gamma r_i}{\|\dot{\mathbf{r}}_i\|} \tag{42}$$

where, in this case, $\Delta t_c = t_c - t$ is determined using Equation (41). The pairwise limiting time-step size, $\Delta t_{ij}^{\lim}$, is computed for all of the potential contact partners as determined by a standard binning algorithm. This is critical to the efficiency of the algorithm since the limiting time-step size is only computed for grains that are near each other. The limiting time-step size that is used at time t is then the minimum of all $\Delta t_{ij}^{\lim}$.

Time-step adaptivity is critical to the efficiency and accuracy of the solution since the system fluctuates greatly over time. In this work two levels of adaptivity are used, the iteration convergence level and the collision interpenetration level. At the iteration convergence level, only the error (see 3(a) in the list below) between successive iterations is computed which costs order N operations. For the collision interpenetration level, the approximate collision times are computed for only grains that are near each other, which depending on the distribution of the grains, is approximately an order N operation. Therefore, the cost of determining the adaptive time-step size for both the first and second levels of adaptivity is negligible compared with the force summation operation for near-field grains. A description of the time-stepping scheme is given in the following list.

[¶] The values of γ and η are usually chosen in the range $0.01 < \gamma < 0.05$ and $0.5 < \eta < 0.9$.

[‖] In this work the surface is a triangular mesh; therefore, the grain–surface collision consists of triangle-sphere contact.

DOI: 10.1002/nme

Summary of time-stepping scheme:

1. Set $k=0$
2. Compute grain positions for $i=1$ to N for the kth iteraton:

$$\mathbf{r}_i^{L+1,k+1} = \frac{\Delta t^2}{m_i}\boldsymbol{\Psi}_i^{\text{tot}}(\mathbf{r}_i^{L+1,k}) + (\mathbf{r}_i^L + \Delta t\dot{\mathbf{r}}_i^L)$$

3. Compute the error for the kth iteration:
   (a) $e^k \stackrel{\text{def}}{=} \frac{\sum_{i=1}^n \|\mathbf{r}_i^{L+1,k} - \mathbf{r}_i^{L+1,k-1}\|}{\sum_{i=1}^n \|\mathbf{r}_i^{L+1,k}\|}$
   (b) $\Phi_k \stackrel{\text{def}}{=} \left(\frac{\left(\frac{Tol}{e^0}\right)^{1/pk_d}}{\left(\frac{e^k}{e^0}\right)^{1/pk}} \right)$
4. If tolerance is met ($e^k \leqslant \text{TOL}$) and $k < k_d$ Then:
   (a) Construct new time step: $\Delta t = \Phi_k \Delta t$
   (b) Compute $\Delta t_{ij}^{\lim}$ for possible collision partners and select $\Delta t^{\lim} = \text{MIN}(\Delta t_{ij}^{\lim})$
   (c) Select minimum: $\Delta t = \text{MIN}(\Delta t^{\lim}, \Delta t)$
   (d) Increment time ($t = t + \Delta t$) and go to (1)
5. If tolerance is not met ($e^k > \text{TOL}$) and $k = k_d$ Then:
   (a) Construct new time step: $\Delta t = \Phi_k \Delta t$
   (b) Restart at time t and go to (1)

5. TIME- AND VOLUME-AVERAGED QUANTITIES

The simulations are performed over a time range T, during this time the system is in a state of fluctuation from one configuration to another. In order to determine the effective response of the system, the observed quantities for each configuration can be averaged in space and time. Time averaging alone can be used to determine the effective response for quantities that are not spatially dependent, for example the total kinetic energy of the system. Volume averaging is used to determine average quantities for a region in space. This can be used with interpolation to build a 'continuous' response of the system. Both time and volume averaging can be used in conjunction to determine an average 'continuous' response. In order to determine average quantities in space, the simulation region is broken up into grid cells. The space is broken up into $N_x N_y N_z$ grid cells, where N_x, N_y, and N_z are the number of grid cells in the x, y, and z directions, respectively. Each grid cell is assigned a set of indices, (i_x, i_y, i_z), and a position, which corresponds to the center of the grid cell. For a quantity Ψ, its average for the grid cell (i_x, i_y, i_z) is

$$\bar{\Psi}_{(i_x,i_y,i_z)} = \frac{1}{N_{(i_x,i_y,i_z)}} \sum_{j=1}^{N_{(i_x,i_y,i_z)}} \Psi_j \tag{43}$$

DOI: 10.1002/nme

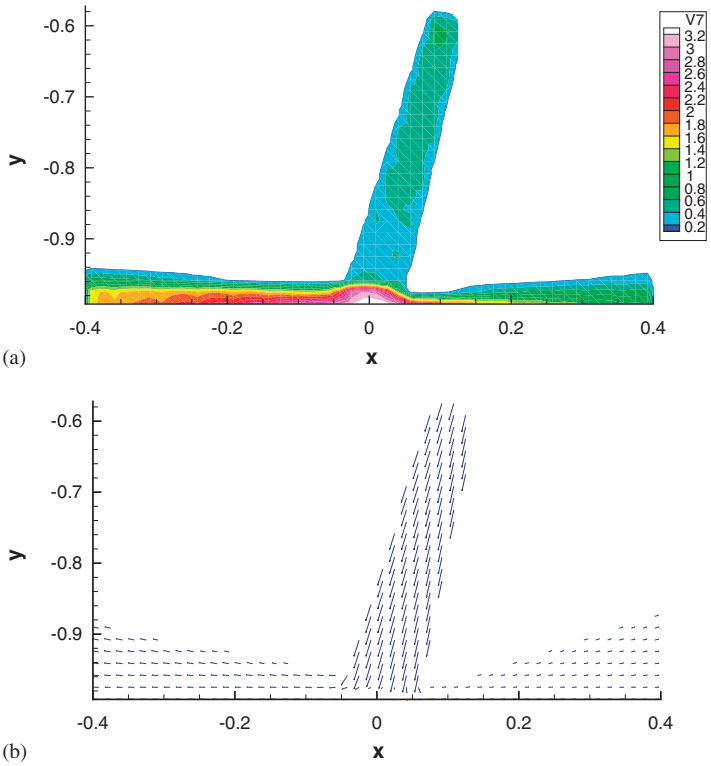

Figure 4. Time and volume averaged: (a) density and (b) velocity.

where $N_{(i_x,i_y,i_z)}$ is the number of grains with their center inside the grid cell with indices (i_x, i_y, i_z), and Ψ_j is the value of the desired quantity for grain j.

In order to determine the effective response in both time and space, volume and time averaging can be used together. At each time, the value of a desired quantity is determined for each grid cell, forming a series of 'snap-shots' of spatially averaged quantities. These 'snap-shots' are then averaged at each grid cell to determine their time average. Figure 4 shows an example of the volume average density and velocity for a granular jet simulation.

6. SURFACE STRESS

Since the grain–surface collisions are modeled through coefficients of friction and restitution there is no measure of the force on the surface during the collision. However, the normal and tangential impulses from each impact can be determined with Equations (26) and (31). Using these impulses, an average surface stress can be defined. In the first part of this section, an analytical solution is presented for the average normal stress on the surface if grain–grain interactions are neglected. In the next section, a description of the numerical algorithm used to measure the averaged surface stress is presented.

DOI: 10.1002/nme

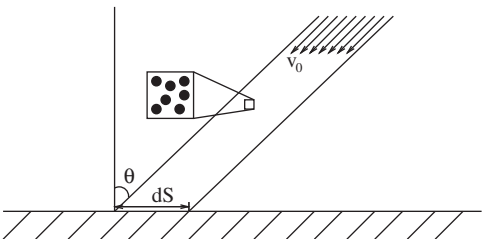

Figure 5. Schematic of a jet striking a surface where the grains do not interact with each other.

6.1. *Non-interacting granular jet*

In order to determine the effect of the grain–grain interactions on the average stress on the surface, first, the average stress from an idealized non-interacting jet is determined. Figure 5 shows a schematic of the non-interacting granular jet, where θ is the angle of attack, $\mathrm{d}S$ is the area of a differential element, and v_0 is the velocity of the jet. The pressure on the surface can be derived using kinetic theory. Let $N(v_0,\theta,m,t)\,\mathrm{d}v_0\,\mathrm{d}\theta\,\mathrm{d}m$ be the number of grains having velocities within $\mathrm{d}v_0$ of v_0, angles within $\mathrm{d}\theta$ of θ, and masses within $\mathrm{d}m$ of m, which approach $\mathrm{d}S$ in time $\mathrm{d}t$. This must equal the volume that contains the grains that approach $\mathrm{d}S$ in time $\mathrm{d}t$ multiplied by the number density of the grains within the velocity, angle, and mass range at time t. This is represented by

$$N(v_0,\theta,m,t)\,\mathrm{d}v_0\,\mathrm{d}\theta\,\mathrm{d}m = v_0\cos(\theta)\,\mathrm{d}S\,\mathrm{d}t \times \frac{N}{V} f(v_0,\theta,m,t)\,\mathrm{d}v_0\,\mathrm{d}\theta\,\mathrm{d}m \tag{44}$$

where $f(v_0,\theta,m,t)\,\mathrm{d}v_0\,\mathrm{d}\theta\,\mathrm{d}m$ is the fraction of grains having velocities within $\mathrm{d}v_0$ of v_0, angles within $\mathrm{d}\theta$ of θ, and masses within $\mathrm{d}m$ of m, and N is the number of grains within volume V at time t. Since it is expected that v_0, θ, and m are independent, then

$$f(v_0,\theta,m,t) = \alpha(v_0,t)\beta(\theta,t)\gamma(m,t) \tag{45}$$

where $\alpha(v_0,t)$, $\beta(\theta,t)$, and $\gamma(m,t)$ are the fraction of grains having velocities within $\mathrm{d}v_0$ of v_0, angles within $\mathrm{d}\theta$ of θ, and masses within $\mathrm{d}m$ of m at time t, respectively. Using Equation (45), Equation (44) can be rewritten as

$$N(v_0,\theta,m,t)\,\mathrm{d}v_0\,\mathrm{d}\theta\,\mathrm{d}m = \frac{N}{V} v_0\cos(\theta)\alpha(v_0,t)\beta(\theta,t)\gamma(m,t)\,\mathrm{d}v_0\,\mathrm{d}\theta\,\mathrm{d}m\,\mathrm{d}S\,\mathrm{d}t \tag{46}$$

The momentum transferred to the surface per unit time per unit area is then given by

$$P_t = \int_{v_0}\int_{\theta}\int_{m} (m(1+e)v_0\cos(\theta))N(v_0,\theta,m,t)\,\mathrm{d}v_0\,\mathrm{d}\theta\,\mathrm{d}m \tag{47}$$

since $m(1+e)v_0\cos(\theta)$ is the normal impulse from a grain–surface collision for a grain of mass m, velocity v_0, angle θ, and a grain–surface coefficient of restitution e. Furthermore, assuming that the number density of the system, N/V, and the grain–surface coefficient of restitution, e, are fixed, then Equation (47) can be rewritten as

$$P_t = \frac{N}{V}(1+e)\int_{v_0}\int_{\theta}\int_{m} m v_0^2\cos^2(\theta)\alpha(v_0,t)\beta(\theta,t)\gamma(m,t)\,\mathrm{d}v_0\,\mathrm{d}\theta\,\mathrm{d}m \tag{48}$$

DOI: 10.1002/nme

Note that the coefficient of restitution is in general dependent on the impact velocity. However in this case it is assumed that the velocity range is small; therefore, e is taken to be constant. For a detailed discussion on the velocity dependence of e, the reader is referred to the work by Goldsmith [34]. Since v_0, θ, and m are independent, then

$$P_t = \frac{N}{V}(1+e)\left[\int_{v_0} v_0^2 \alpha(v_0,t)\,\mathrm{d}v_0\right]\left[\int_{\theta} \cos^2(\theta)\beta(\theta,t)\,\mathrm{d}\theta\right]\left[\int_{m} m\gamma(m,t)\,\mathrm{d}m\right] \tag{49}$$

and assuming that $\alpha(v_0,t)$, $\beta(\theta,t)$, and $\gamma(m,t)$ are independent of time, the normal pressure on the surface is given by

$$P = \bar{\rho}(1+e)\bar{v_0^2}\left[\int_{\theta} \cos^2(\theta)\beta(\theta)\,\mathrm{d}\theta\right] \tag{50}$$

where $\bar{\rho} = N\bar{m}/V$ is the average density and $\bar{v_0^2}$ is the mean square velocity of the flow. For constant v_0, m, and θ Equation (50) reduces to $P = \rho(1+e)v_0^2\cos^2(\theta)$.

6.2. *Interacting granular jet*

Using the simulation described in Section 2 the average stress on the surface can determined for a number of parameters. As described above, the normal and tangential impulses from each impact can be determined with Equations (26) and (31). By computing these impulses for each impact, the average stress for a given time period can be determined over a patch on the surface. If this is done over the entire surface it provides information about the profile of stresses as a function of the position. The average stress for a patch with area A over a total time T is given by

$$\begin{aligned} \mathbf{N}(T) &= \frac{\sum_i (\overline{f}_n \delta t)_i \mathbf{n}_i}{\mathrm{TA}} \\ \mathbf{S}(T) &= \frac{\sum_i (\overline{f}_t \delta t)_i \mathbf{t}_i}{\mathrm{TA}} \end{aligned} \tag{51}$$

where $\mathbf{n}_i$ and $\mathbf{t}_i$ are the normal and tangential unit vectors for collision i, respectively, and $(\overline{f}_n \delta t)_i$ and $(\overline{f}_t \delta t)_i$ are the projections of the impulse in the normal and tangential directions, respectively. Figure 6 shows an example for the normal and tangential stresses on a surface from a three-dimensional simulation. The surface is divided into grid cells and Equation (51) is used to determine the average surface stress for each cell over a time interval T. In order to measure the uncertainty in the stress calculation, the total time interval T is divided into the sub-intervals of time $T_n = T/n_T$. For each sub-interval the surface stress is computed using Equation (51) at every grid cell. This gives n_T values of the surface stress at different time intervals for each cell. The reported value of the stress for cell j over the n_T samples is the mean value over the n_T samples. For example, for the normal stress the mean value is

$$\bar{\mathbf{N}}^j = \frac{\sum_{n=1}^{n_T} \mathbf{N}^j(T_n)}{n_T} \tag{52}$$

where T_n corresponds to the n'th time interval. The reported uncertainty in the solution is the standard deviation of the mean over each cell j. Invoking the central limit theorem, the variance

DOI: 10.1002/nme

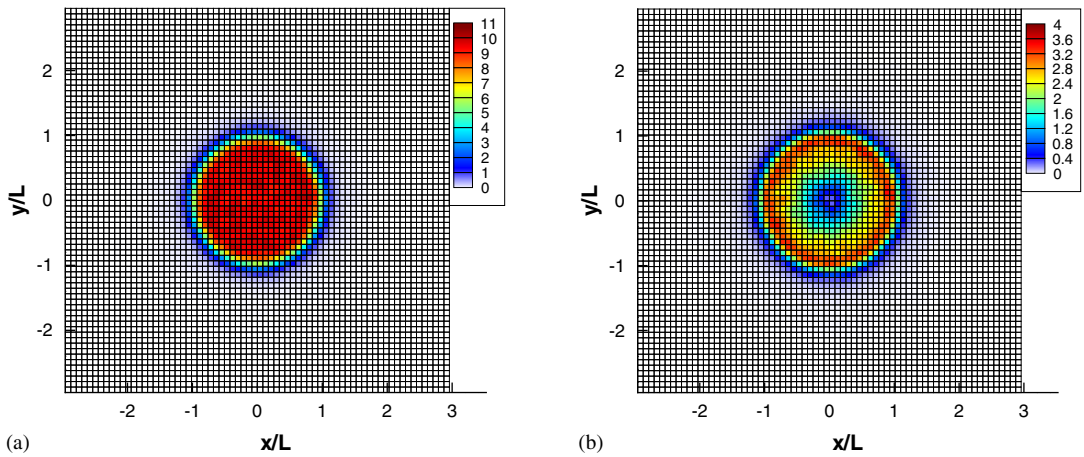

Figure 6. Example of a surface stress calculation in three dimensions for: (a) the normal stress and (b) the shear stress, with the units of KPa. Each grid cell corresponds to the area over which the averaging is performed.

in the sample mean is the variance over all samples divided by the number of samples; therefore, the reported uncertainty in the normal stress is

$$\Delta \mathbf{N}^j = \frac{\sqrt{\sum_{n=1}^{n_T} (\mathbf{N}^j(T_n) - \bar{\mathbf{N}}^j)^2}}{n_T} \tag{53}$$

6.3. Normalized surface stress

In order to determine the relative effect of the grain–grain interactions on the surface stress, a normalized stress measure is introduced. This is the ratio of the measured stress, as described in Section 6.2, to the stress from a non-interacting granular jet, as described in Section 6.1. For the normalized normal stress, the average normal stress is scaled by the pressure from the non-interacting granular jet, whereas the normalized shear stress is scaled by the product of the pressure and the static coefficient of friction. Note that normalization by the static coefficient of friction is a somewhat arbitrary choice since the dynamic coefficient of friction or a weighted average of the static and dynamic coefficients of friction could be used. Using Equation (50) the normalized normal and shear stresses for grid cell j are given by

$$\hat{\mathbf{N}}^j = \frac{\bar{\mathbf{N}}^j}{\bar{\rho}(1+e)\bar{v}_0^2[\int_\theta \cos^2(\theta)\beta(\theta)\,\mathrm{d}\theta]}$$

$$\hat{\mathbf{S}}^j = \frac{\bar{\mathbf{S}}^j}{\mu\bar{\rho}(1+e)\bar{v}_0^2[\int_\theta \cos^2(\theta)\beta(\theta)\,\mathrm{d}\theta]} \tag{54}$$

where $\bar{\mathbf{S}}^j$ is computed in the same way as $\bar{\mathbf{N}}^j$ using Equation (52).

DOI: 10.1002/nme

7. PARAMETER STUDIES FOR TWO-DIMENSIONAL SURFACE STRESS CALCULATIONS

Parameter studies are conducted for two-dimensional examples to determine the effect of different parameters on the surface stress. In this case the normalized surface stress is computed in order to determine how the parameters influence the surface stress through the grain–grain interactions. The effect of the following parameters will be examined: the angle of attack θ, the strength of the near-field forces, the flow velocity v_0, the volume fraction at the inflow region $\alpha = \bar{\rho}/\bar{m}$, and the grain–surface coefficient of restitution. For the examples, the following base values for the parameters are used: $\theta = 30°$, $\alpha = 0.1$, the flow velocity is uniform with $v_0 = 20\,\mathrm{m/s}$, the grain–grain coefficient of restitution is $e = 0.3$, the grain-wall coefficient of restitution is $e_w = 0.3$, and the static and dynamic coefficients of friction for both the grain–grain and grain–surface interactions are $\mu_s = 0.3$ and $\mu_d = 0.2$. For each example the base values are used for all of the parameters except for the parameter that is being varied within that example.

Figure 7 shows the effect of the near-field force strength on the normalized normal ($\hat{\mathbf{N}}$) and shear ($\hat{\mathbf{S}}$) stresses. For this analysis, the near-field coefficients in Equation (3) are chosen such that $\beta_1 = 2$ and $\beta_2 = 3$ are constant and $\alpha_1/\alpha_2 = 0.002$ is constant. The magnitude of the near-field forces is varied by varying α_1 and therefore α_2 by the ratio r_c, where $\alpha_1 = r_c \alpha_0$. With this choice of parameters, the magnitude of the forces is clearly proportional to r_c. For these examples α_0 is chosen such that $\alpha_0/\bar{m} = 5.0 \times 10^{-4}$, where $\bar{m}$ is the average mass of the grains. For this choice of parameters, it is seen from Figure 7 that the near-field forces have the effect of reducing the peak stresses on the surface but increasing the size of the region with non-zero stresses. This effect is largely dependent on the equilibrium distance between the grains. For this case, the near-field parameters cause the granular jet to spread out, this leads to the 'spreading' of the surface stress profile. However, if the near-field parameters are chosen so that the granular jet agglomerates, one would expect that the profile would become narrower as r_c increases.

For the remaining examples in this section near-field effects are neglected. The first of these examples investigates how the angle of attack, θ, affects the normalized normal ($\hat{\mathbf{N}}$) and shear

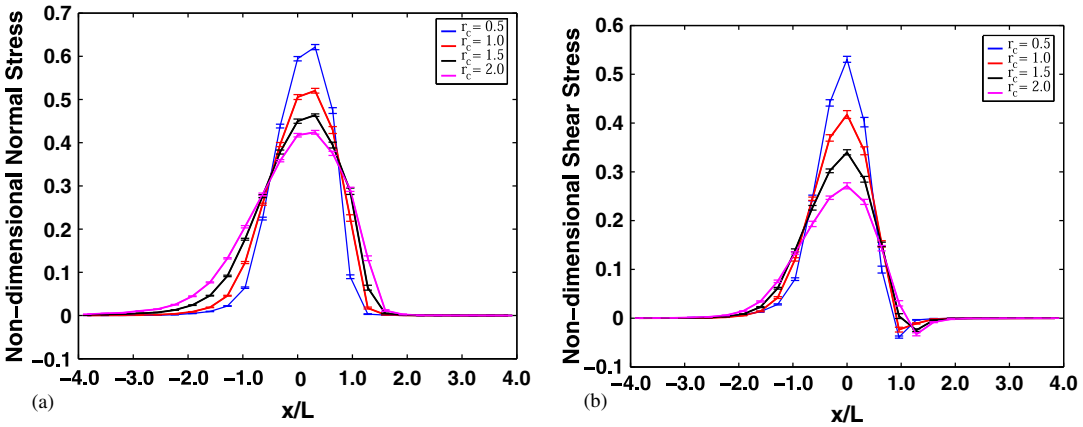

Figure 7. Normalized: (a) normal stress and (b) shear stress as a function of the near-field strength ratio r_c.

DOI: 10.1002/nme

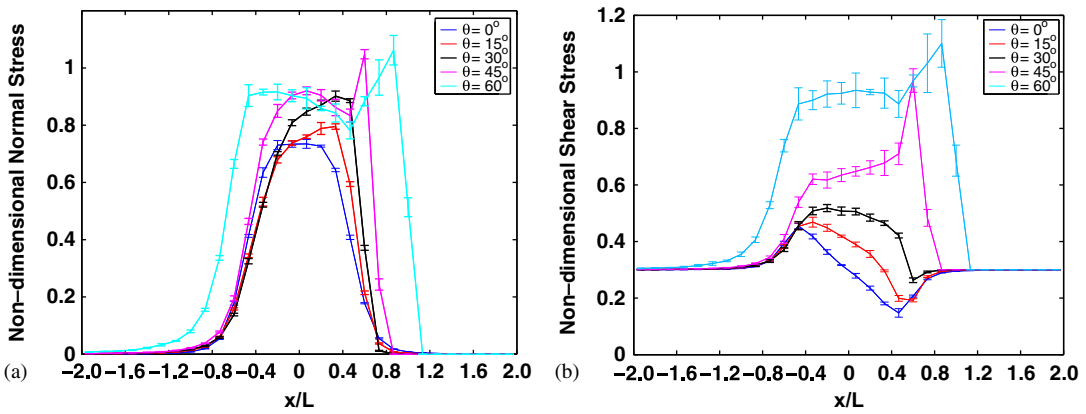

Figure 8. Normalized: (a) normal stress and (b) shear stress as a function of angle of attack.

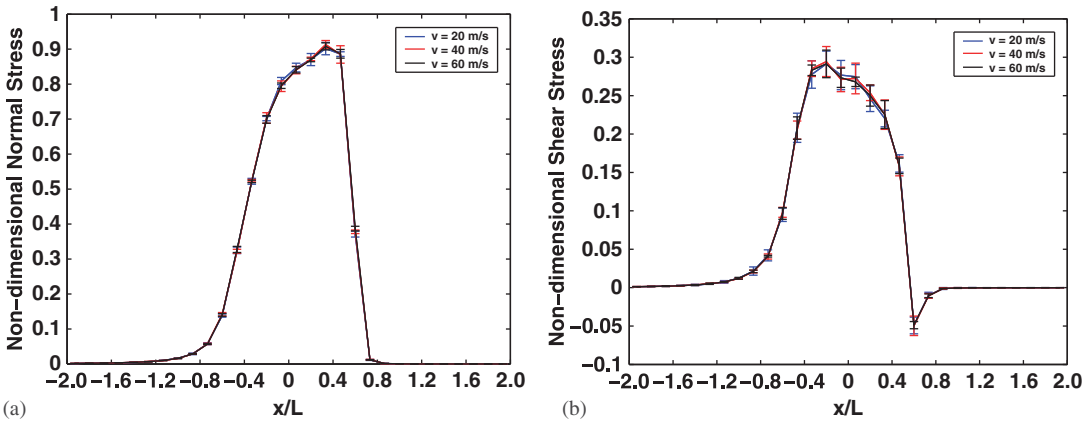

Figure 9. Normalized: (a) normal stress and (b) shear stress as a function of velocity.

($\hat{\mathbf{S}}$) stresses (Figure 8). For $\theta = 0°$ the normal and shear stresses are symmetric as expected. The shear stress is positive in the region where the grains flow in the positive direction and negative in the region where the grains flow in the negative direction. Initially, as θ is increased, more material flows to the left than to the right. This causes an increase in the positive shear stress, while the negative part of the shear stress vanishes. Also, by increasing the angle of attack the contact area widens, and therefore the grain–grain interactions decrease. This is seen in Figure 8 as an increase in the magnitude of the normalized normal and shear stresses with increasing θ. As θ is further increased, there comes a point where the grains moving toward the surface are not deflected by grains rebounding from the surface. At this point, the grains in that region should exert a normal and shear stress equivalent to that of the non-interacting granular jet. This is seen in Figure 8 for $\theta = 45°$ and $\theta = 60°$, where $\|\hat{\mathbf{N}}\| \approx 1$ and $\|\hat{\mathbf{S}}\| \approx 1$ in the region where the grains do not interact with each other.

DOI: 10.1002/nme

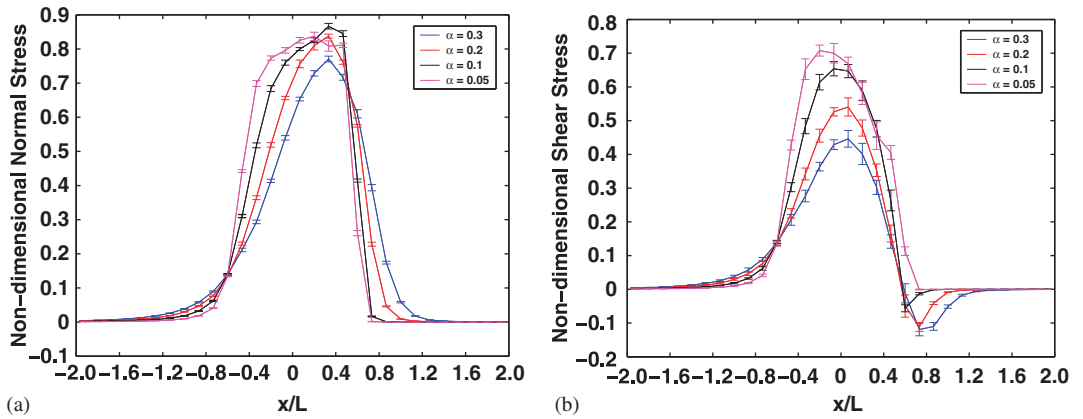

Figure 10. Normalized: (a) normal stress and (b) shear stress as a function of the particulate volume fraction.

Figure 9 shows the effect of varying the flow velocity, v_0, on the normalized normal and shear stresses. The simulations are carried out for three different velocities. From Figure 9 it is apparent that the normalized stress is independent of velocity. In this simulation the coefficient of restitution was assumed to be a constant. In general, the coefficient of restitution depends on the velocity at impact. Clearly, if this velocity dependence were included in the model the normalized stresses would depend on the velocity.

Figure 10 shows the effect of varying the volume fraction of grains, α, on the normalized stresses. As the volume fraction decreases, the grain–grain interaction decreases as well. It would be expected that with decreasing volume fraction, the stress would approach that of the ideal non-interacting case. In this case the pressure is constant in the impact region and vanishes outside of this region, resembling a square wave. In Figure 10 it is seen that as α decreases, the normalized stresses increase and start to 'flatten' out. While at high values of α the stresses are fairly peaked, at low values of α they become more flat in the impact region.

Figure 11 shows the effect of varying the grain–surface coefficient of restitution, e_w, on the normalized stresses. In Figure 11 the stress is seen to increase with decreasing grain–surface coefficient of restitution. As the coefficient of restitution decreases, the grains rebound with less energy from the surface. In turn, these grains have less effect on reducing the kinetic energy of grains approaching the surface.

8. PARAMETER STUDIES FOR THREE-DIMENSIONAL SURFACE STRESS CALCULATIONS

In this section, a three-dimensional example is presented where the angle of attack is varied for a nozzle with a circular cross-section. For this example, the following parameters are used: $\alpha = 0.1$, the grain–grain coefficient of restitution is $e = 0.3$, the grain-wall coefficient of restitution is $e_w = 0.3$, and the static and dynamic coefficients of friction for both the grain–grain and grain–surface interactions are $\mu_s = 0.3$ and $\mu_d = 0.2$. The flow velocity is chosen such that the velocity is in the direction of the axis of the jet along the center of the jet and spreads with an angle

DOI: 10.1002/nme

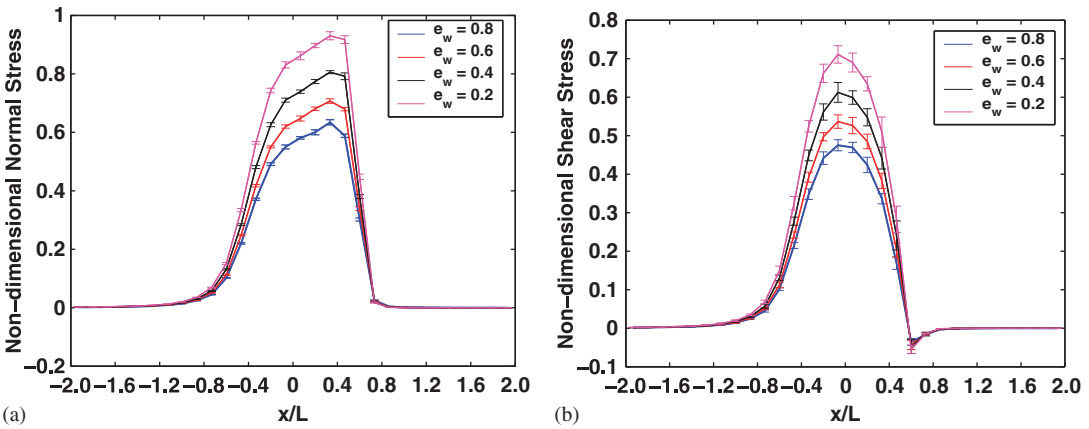

Figure 11. Normalized: (a) normal stress and (b) shear stress as a function of the grain–surface coefficient of restitution.

$\phi=(2\xi/L)\phi_o$ from the axis at a radial distance ξ from the center of the jet, where L is the diameter of the jet and $\phi_o=4°$ is used for this example. The magnitude of the velocity is chosen to be 20 m/s everywhere. Figure 12 shows the normalized stress patterns for $\theta=0°$. In this case, the stress patterns are radially symmetric as would be expected. For the given process parameters, the normal stress is nearly constant in the region directly under the nozzle and quickly decays outside of this region. The normalized shear stress is nearly zero at the center, this is the region where the tangential impact velocity of the grains is nearly zero. The shear stress increases as the radial distance from the center increases, it then reaches a maximum and decreases to zero as the radial distance from the center increases further. Figure 13 shows the stress patterns for $\theta=10°$. In this case, the normalized normal stress slightly increases in the effective region as x/L increases. When compared with the $\theta=0°$ case, the region where normalized shear stress vanishes is located at a higher x/L value. The shear stress is maximized near the negative x/L edge of the effective stress region. Figure 14 shows the stress patterns for $\theta=20°$. Once again, the normalized normal stress slightly increases in the effective region as x/L increases and reaches a maximum at the positive x/L edge. With the higher angle of attack, there no longer exists a region where normalized shear stress vanishes inside of the effective stress region. When compared with the $\theta=10°$ case, the maximum shear stress is located at a higher x/L value. Figure 15 shows the stress patterns for $\theta=30°$. In this case, the normalized normal stress is nearly constant throughout the effective region except at the positive x/L edge where it reaches a maximum. The normalized shear stress also reaches a maximum near the positive x/L edge, then decays rapidly as x/L decreases to reach a nearly constant value throughout the rest of the effective region. Note that there are larger stress variation in y direction at these values of θ. Finally, Figure 16 shows the stress patterns for $\theta=60°$. Here, the normalized normal and shear stresses show the same patterns. They achieve a maximum near the positive x/L edge of the effective region, then decay rapidly as x/L decreases to reach a nearly steady value, and then continue to decrease further as x/L is further decreased. Note that for θ between 40 and 60° similar trends in the stress appear, with the exception that the effective region is stretched in the x direction as θ increases.

DOI: 10.1002/nme

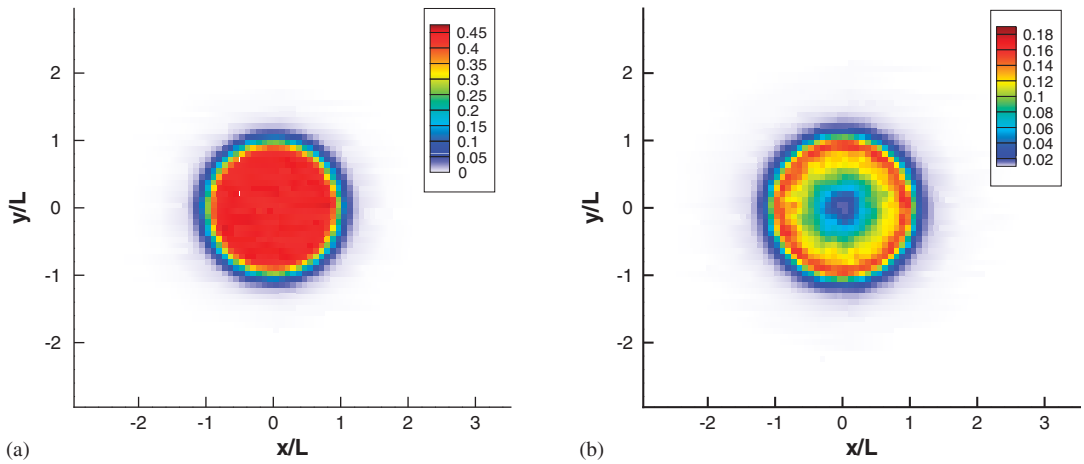

Figure 12. Normalized: (a) normal stress and (b) shear stress for $\theta = 0°$.

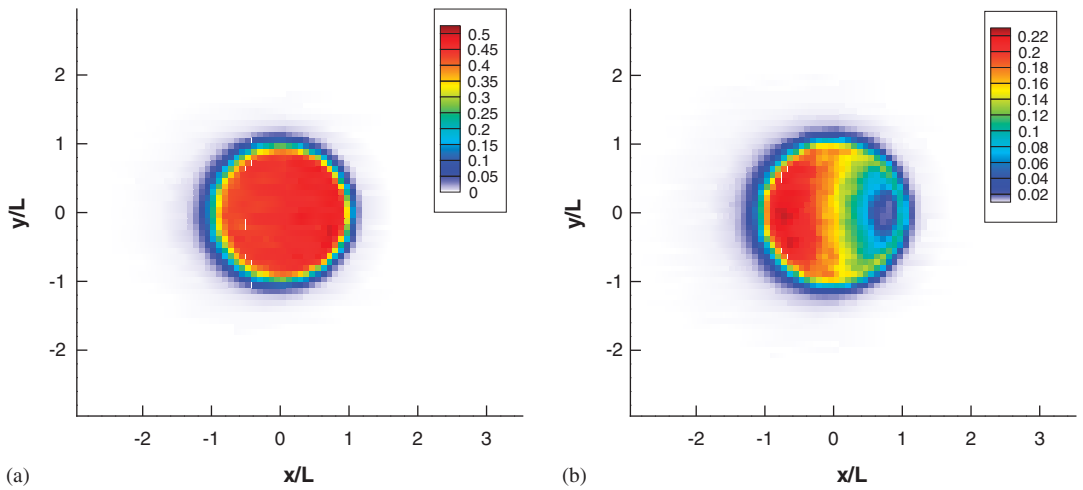

Figure 13. Normalized: (a) normal stress and (b) shear stress for $\theta = 10°$.

9. OUTFLOW CALCULATIONS

In order to determine quantities such as momentum, energy, or mass flux at the outflow region, the position, mass, and velocity of a grain are recorded when the grain leaves the outflow box. The outflow region is divided into grid cells and for a time period T and grid size Δh the quantity of interest Ψ is time and volume averaged as

$$\bar{\Psi}'(\Delta h_i) = \frac{\sum_{j=1}^{N_i} \Psi_j(\Delta h_i)}{T} \tag{55}$$

DOI: 10.1002/nme

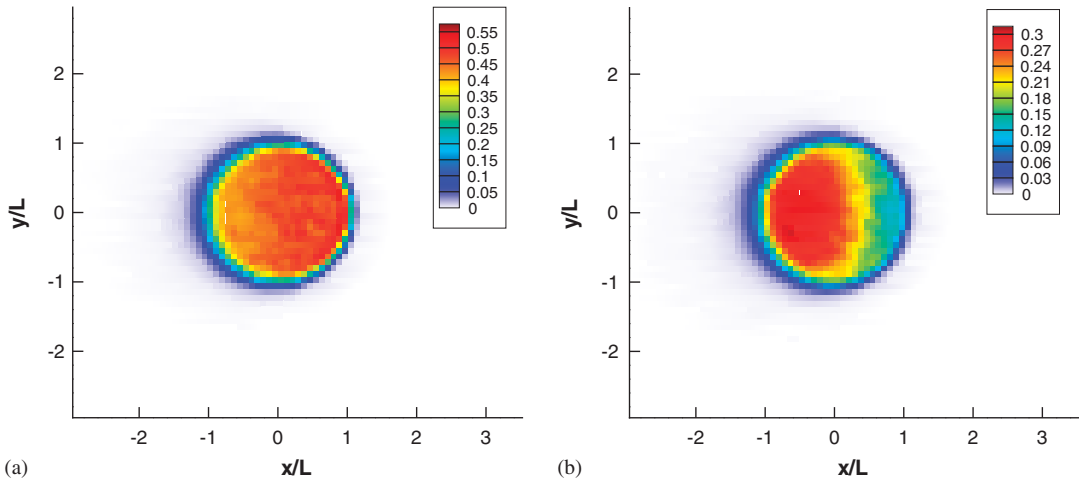

Figure 14. Normalized: (a) normal stress and (b) shear stress for $\theta = 20°$.

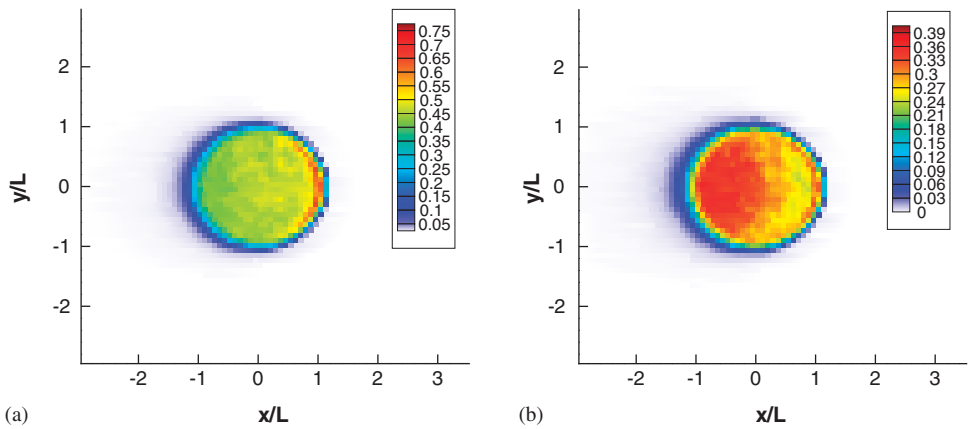

Figure 15. Normalized: (a) normal stress and (b) shear stress for $\theta = 30°$.

where $\bar{\Psi}'(\Delta h_i)$ is the rate of the time-averaged quantity for grid Δh_i, $\Psi_j(\Delta h_i)$ is the quantity of interest for grain j that crossed grid Δh_i, and N_i is the number of grains that crossed grid Δh_i in the time period T. The outflow profile is determined by using Equation (55) on all of the individual outflow cells. In order to measure the uncertainty in the outflow calculation, the total time interval T is divided into sub-intervals of time $T_n = T/n_T$. For each sub-interval the outflow quantity is computed using Equation (55) at every grid cell. This gives n_T values of the outflow quantity at different time intervals for each cell. The reported value of the outflow quantity for cell i over the n_T samples is the mean value over the n_T samples

$$\langle \bar{\Psi}'(\Delta h_i) \rangle = \frac{\sum_{n=1}^{n_T} \bar{\Psi}'(\Delta h_i, T_n)}{n_T} \tag{56}$$

DOI: 10.1002/nme

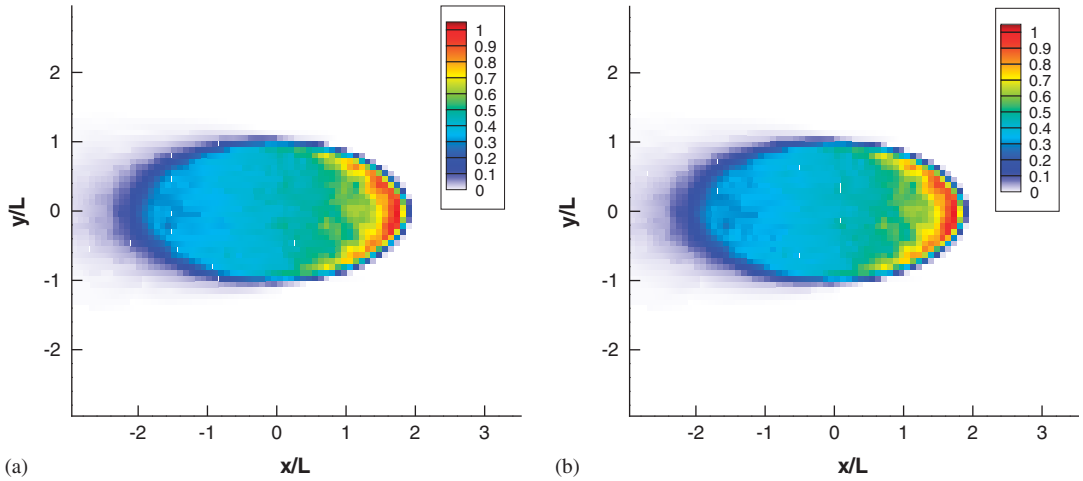

Figure 16. Normalized: (a) normal stress and (b) shear stress for $\theta = 60°$.

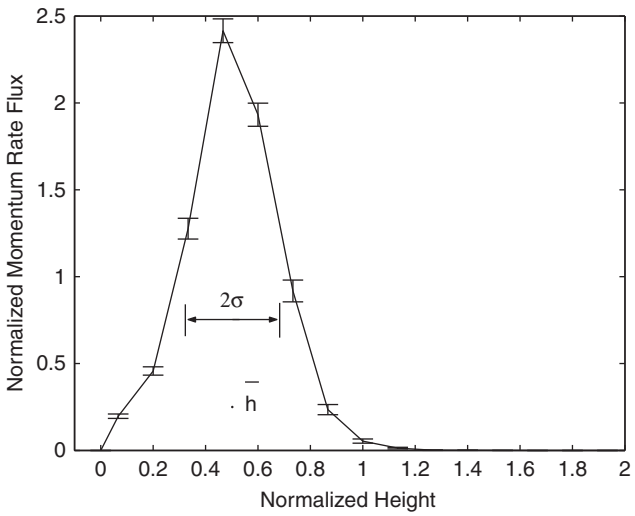

Figure 17. Rate of momentum flux along with its normalized centroid $\overline{h}$ and the second moment σ.

where T_n corresponds to the n'th time interval. The reported uncertainty in the solution is the standard deviation of the mean over each cell j

$$\Delta\bar{\Psi}'(\Delta h_i) = \frac{\sqrt{\sum_{n=1}^{n_T}(\bar{\Psi}'(\Delta h_i, T_n) - \langle\bar{\Psi}'(\Delta h_i)\rangle)^2}}{n_T} \tag{57}$$

where, as with Equation (53), the central limit theorem was used to derive Equation (57). Figure 17 shows the normalized value of $\langle\bar{\Psi}'(h)\rangle$ as a function of the normalized height h/L from the

DOI: 10.1002/nme

surface, where L is the width of the granular jet as depicted in Figure 1, and the normalization value is a constant which will be defined in Equation (58). Here, $\langle\bar{\Psi}'(h)\rangle = \mathbf{I}[\langle\bar{\Psi}'(\Delta h_i)\rangle]$, where $\mathbf{I}[\cdot]$ is an operator that takes the data at each grid cell and returns a piecewise continuous function by linearly interpolating the desired quantity between cells. In Figure 17 a normalized value of $\langle\bar{\Psi}'(h)\rangle$ is shown, where the normalization factor R is given by

$$R = \int_0^\infty \langle\bar{\Psi}'(h)\rangle \, \mathrm{d}h \tag{58}$$

In the example shown in Figure 17, $\Psi = mv_x$ is the momentum flux through the left side of the outflow box in the $\mathbf{e}_1$ direction, as shown in Figure 1.

In order to characterize the outflow conditions of a quantity Ψ with a statistical measure, the second and third statistical moments of $\langle\bar{\Psi}'(h)\rangle$ are computed. First, the expected value of h/L is computed as

$$\bar{h} = \frac{\int_0^\infty h\langle\bar{\Psi}'(h)\rangle \, \mathrm{d}h}{LR} \tag{59}$$

this value represents the centroid of the flux of Ψ, $\bar{h}$ is shown for $\Psi = mv_x$ in Figure 17. The normalized second moment is computed as

$$\sigma^2 = \frac{\int_0^\infty (h-\bar{h})^2\langle\bar{\Psi}'(h)\rangle \, \mathrm{d}h}{L^2 R} \tag{60}$$

this value represents the spread of the quantity Ψ of the granular jet at the outflow region. Figure 17 shows the value σ for $\Psi = mv_x$. The normalized third moment is computed as

$$\kappa = \frac{\int_0^\infty (h-\bar{h})^3\langle\bar{\Psi}'(h)\rangle \, \mathrm{d}h}{L^3 R} \tag{61}$$

where κ/σ^3 represents the skewness of the quantity Ψ of the granular jet at the outflow region. The uncertainties in R, $\bar{h}$, σ, and κ are computed using a Monte Carlo approach.

10. PARAMETER STUDIES FOR OUTFLOW CALCULATIONS

In this section, the effect of the surface morphology and the near-field interaction between the grains on the rate of flux of momentum through the outflow region is investigated for two-dimensional simulations. The rate of momentum flux across an interface can be interpreted as being proportional to the force that would act on the interface if it was replaced by a solid surface. Therefore, the profile, as shown in Figure 17, represents how the force that would be exerted on a surface varies with height. For this case, R is a quantity which is proportional to the total force and $\bar{h}$ is the centroid of the force that would be exerted on a surface. For the examples in the remainder of this section, the following parameters are used: $\theta = 30°$, $\alpha = 0.1$, $v_0 = 20\,\mathrm{m/s}$, the grain–grain coefficient of restitution is $e = 0.3$, the grain-wall coefficient of restitution is $e_w = 0.3$, and $\mu_s = 0.3$ and $\mu_d = 0.2$.

In this example, the effect of varying the magnitude of the grain–grain near-field forces on the moments of the rate of momentum flux is investigated. For this analysis, the near-field coefficients

DOI: 10.1002/nme

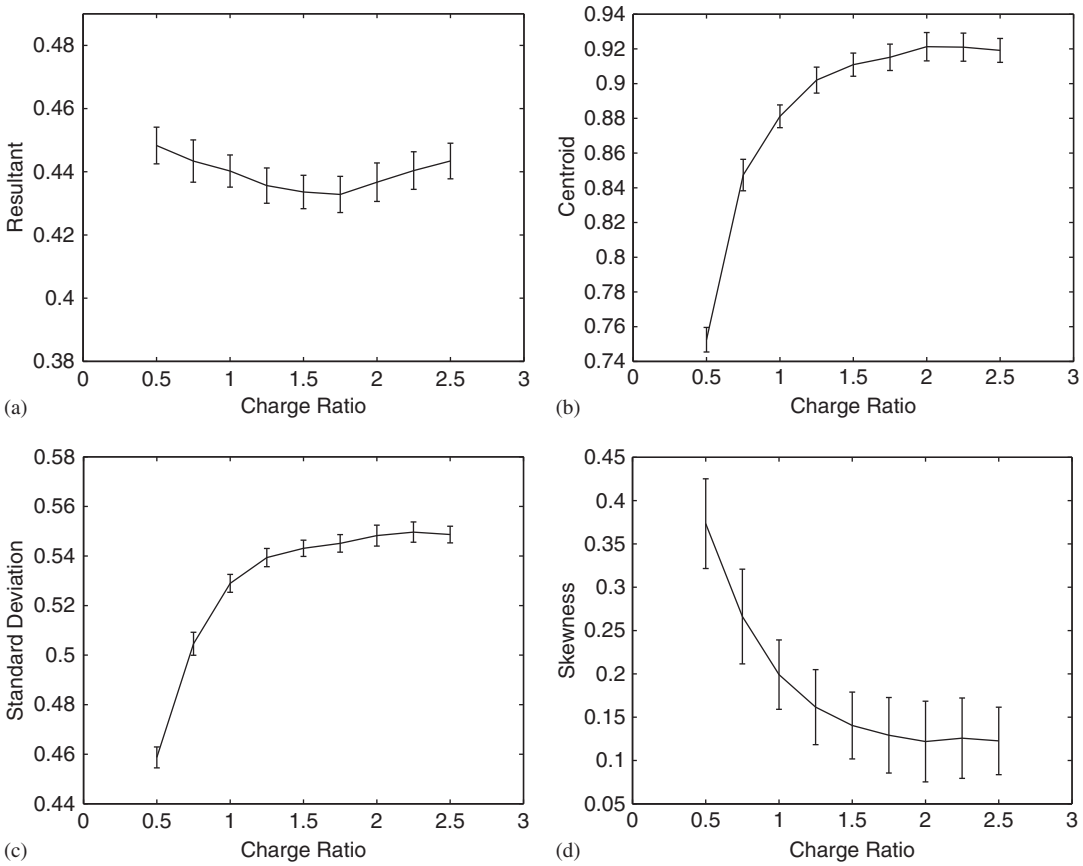

Figure 18. Variation of moments as a function of the near-field forces between grains.

in Equation (3) are the same as those used for the near-field grain–surface stress example in Section 7. Figure 18 shows the variation of the moments as a function of r_c for the rate of momentum flux. Sub-figure (a) shows that the resultant decreases slightly as the magnitude of the near-field forces is increased then reaches a minimum and increases once again as r_c is further increased. However, this variation is fairly weak and the total variation of the resultant over the range of r_c chosen is close to that of the uncertainty in R. Therefore, the resultant of the rate of momentum flux across the outflow interface is fairly insensitive to r_c for the entire range used in this example. Figure 18(b) shows the effect r_c on the centroid, $\bar{h}$. At first, the centroid increases rapidly as r_c increases until it reaches a point where the centroid remains fairly constant with a further increase of r_c. For the range of r_c used in this example, $\bar{h}$ is very sensitive to changes in r_c for $r_c<1.5$ and fairly insensitive to changes in r_c for $r_c>1.5$. Figure 18(c) shows the effect r_c on the spread of the granular jet at the outflow region, which is characterized by σ. Similarly to the trend of the centroid, σ increases rapidly as r_c increases until it reaches a point where it remains fairly constant with a further increase of r_c. Clearly, the spread of the granular jet and the

DOI: 10.1002/nme

centroid is closely related. As the flow spreads out, the centroid must increase since the surface prevents the grains from spreading in the downward direction. Figure 18(d) shows the effect r_c on the skewness of the outflow profile, κ/σ^3. At first, the skewness decreases rapidly with increasing r_c until it reaches a point where it remains nearly constant as r_c is increased further. The skewness remains positive for the entire range of r_c used in this example. Positive skewness corresponds to the profile of the outflow having a longer tail in the direction of increasing height. As was the case with $\bar{h}$, it is expected that the skewness decreases since there is more space for the grains to flow out between the surface and the centroid of the flow.

For the next example, the effect of surface morphology on the moments of the rate of momentum flux is examined. For this case, no near-field effects are considered. The surface is modeled as a periodic surface that is parametrized by its amplitude A and wavelength λ. Figure 19 shows a schematic of the surface that is constructed with a sinusoidal function. For this analysis, two different parameter studies are considered. For the first study, the normalized amplitude, $\hat{A} \stackrel{\text{def}}{=} A/L$, is held fixed while the number of asperities, $n_a \stackrel{\text{def}}{=} L/\lambda$ is varied, where L is the width of the jet (see Figure 1). For the second study, n_a is varied while $\hat{A}$ is fixed.

Figure 20 shows the variation of the moments as a function of n_a for the rate of momentum flux. Sub-figure (a) shows the effect on the resultant, R. The resultant decreases as n_a is increased then reaches a nearly constant value. This is expected, since as the surface becomes rougher, more energy is removed from the grains. This decrease occurs more rapidly for smaller values of n_a and then tends to level off for higher values of n_a. Therefore, the resultant of the rate of momentum flux across the outflow interface is more sensitive for small n_a than for large n_a. Figure 20(b) shows the effect n_a on the centroid, $\bar{h}$. The centroid is seen to increase at a fairly constant rate with respect to n_a. The first point in Figure 20 ($n_a = 0$) corresponds to a perfectly flat surface. Clearly, there is a large change between a perfectly flat surface and the first non-zero data point of n_a. It is expected that the results approach those of a flat surface as $n_a \to 0$ and $\hat{A} \to 0$. For values of $n_a < 2$, $\bar{h}$ is very sensitive to changes in n_a and is less sensitive as n_a is further increased. Figure 20(c) shows the effect n_a on σ. As was seen with the sensitivity of $\bar{h}$ and σ to r_c, the centroid and spread of the flow are closely related. Here, $\bar{h}$ and σ show similar trends of a nearly constant increase in σ as n_a is increased for $n_a > 2$. Figure 20(d) shows the effect n_a on the skewness of the outflow profile. The skewness decreases with increasing n_a at a fairly constant rate for $n_a > 2$. The skewness is positive for $n_a < 10$ and negative for $n_a > 12$, this corresponds to an outflow profile

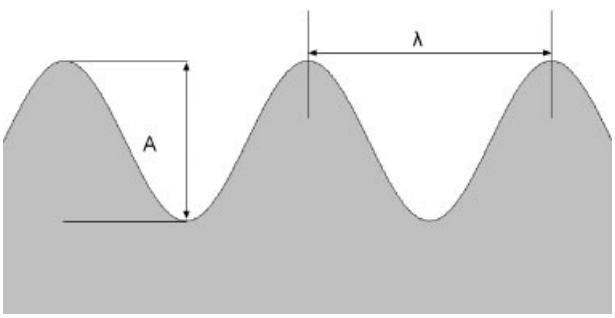

Figure 19. Schematic of surface morphology showing its amplitude A and wavelength λ.

DOI: 10.1002/nme

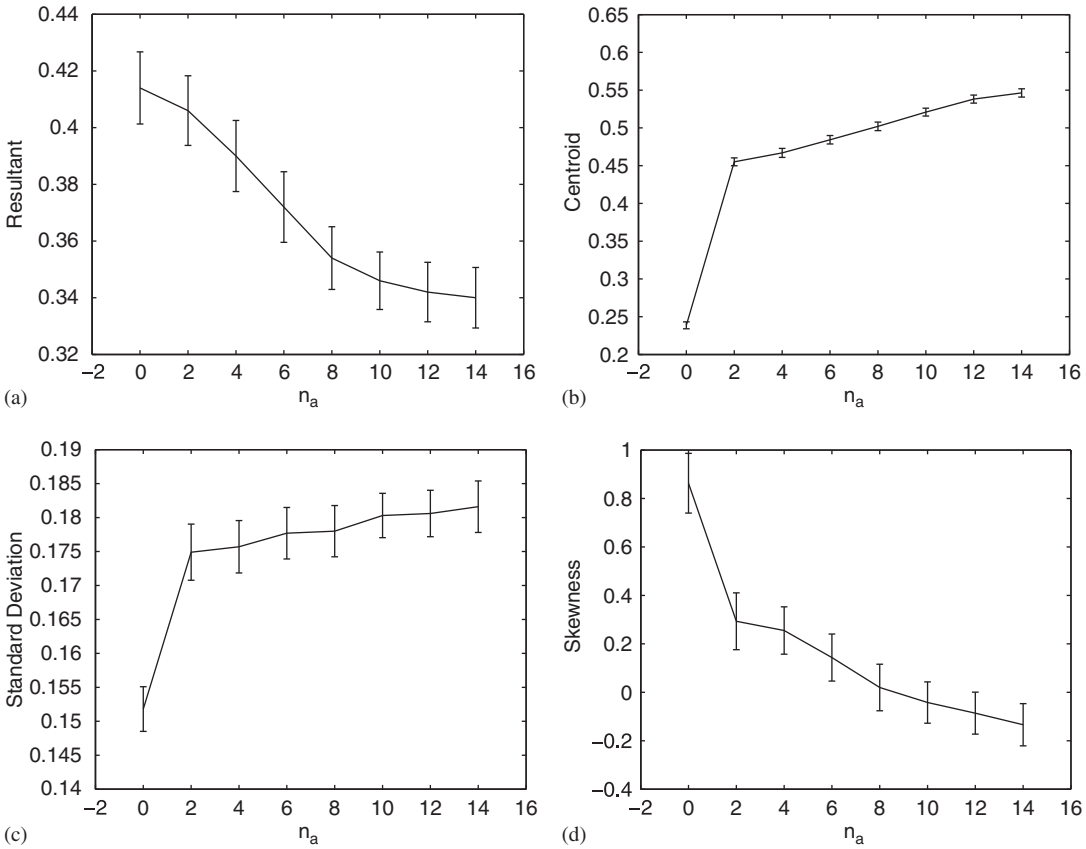

Figure 20. Variation of moments as a function of the number of asperities on the surface.

having a longer tail in the direction of increasing height for $n_a<10$ and a longer tail in the direction of decreasing height for $n_a>12$.

Figure 21 shows the variation of the moments as a function of the normalized amplitude, $\hat{A}$, for the rate of momentum flux. Sub-figure (a) shows that at first the resultant decreases as $\hat{A}$ is increased and then R reaches a nearly constant value as $\hat{A}$ is further increased. Therefore, the resultant is highly sensitive to changes in the height of the asperities up to a certain height at which point it becomes insensitive to further changes in $\hat{A}$. As the height of the asperities is increased beyond a critical point the grains become stagnant in between the asperities and fill the asperities. After this point, any changes in the height of the asperities have no effect on the outflow of the grains. Figure 21(b) shows that the centroid increases rapidly with increasing $\hat{A}$ at first and less rapidly as $\hat{A}$ is further increased. It is also noted that as $\hat{A}\to 0$, $\bar{h}$ approaches the value obtained from a perfectly flat surface that corresponds to $\hat{A}=0$ in Figure 21(b). Figure 21(c) shows that σ has a similar trend to $\bar{h}$ as $\hat{A}$ is varied. However, while $\bar{h}$ keeps increasing slightly for $\hat{A}>0.04$, σ remains nearly constant for this range of $\hat{A}$. Figure 21(d) shows that the skewness decreases with increasing $\hat{A}$ for $\hat{A}<0.04$ and is nearly constant for $\hat{A}>0.04$.

DOI: 10.1002/nme

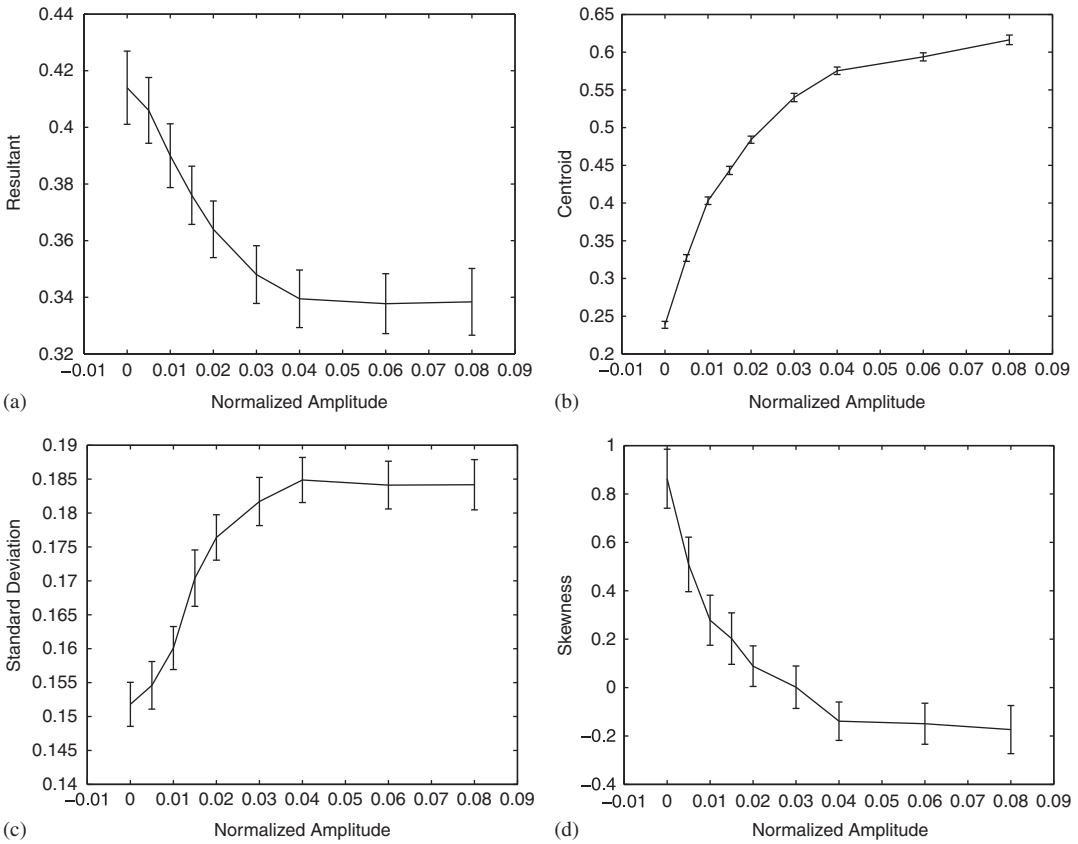

Figure 21. Variation of moments as a function of the normalized amplitude on the surface.

11. CONCLUDING REMARKS

In this paper a simulation of near-field granular jets impinging on a surface was developed, and an analysis of the following three areas was performed: (1) volume-averaged quantities; (2) surface tractions; and (3) outflow conditions. In particular, the analysis of surface tractions has tangible applications for industrial processes. For blast cleaning applications, Ciampini *et al.* [32] performed parametric studies to determine how particle interference affects the amount of power that is transmitted to the surface with respect to the total power available. Their parametric studies were performed at lower grain volume fractions than those reported here, but similar trends were found in this work. For example, they found that increasing the grain–surface coefficient of restitution decreased the amount of power transferred to the surface as is evident here from Figure 11. Another application of the surface stress profile calculations is the generation of desired surface geometries, for example using abrasive jet micromachining (see [38] and [39]). The surface stress patterns could be used to predict the initial surface geometry. Conversely, an inverse problem could be solved to generate a desired surface from a range of possible flow parameters. For example, the large variations in the stress profiles for varying angle of attack could be used to generate a range

DOI: 10.1002/nme

of geometries on a surface. Zohdi [27–30] has dealt with the solution of inverse problems in granular flow applications using genetic algorithms. These same techniques could be used to deal with these granular jet applications.

ACKNOWLEDGEMENTS

This work is supported by a grant from the National Science Foundation under Grant No. DMI-20062085 as part of the Consortium on Deburring and Edge Finishing (CODEF) at the University of California, Berkeley. This work was also in part funded by the Alfred P. Sloan Foundation Minority PhD Program.

REFERENCES

1. Behringer RP. The dynamics of flowing sand. *Nonlinear Science Today* 1993; **3**:1.
2. Behringer RP, Baxter GW. Pattern formation, complexity and time-dependence in granular flows. In *Granular Matter—An Interdisciplinary Approach*, Mehta A (ed.). Springer: New York, 1993; 119–185.
3. Behringer RP, Howell D, Veje C. Fluctuations in granular flows. *Chaos* 1999; **9**:559–572.
4. Tai Y-C, Noelle S, Gray JMNT, Hutter K. Shock capturing and front tracking methods for granular avalanches. *Journal of Computational Physics* 2002; **175**:269–301.
5. Tai Y-C, Gray JMNT, Hutter K, Noelle S. Flow of dense avalanches past obstructions. *Annals of Glaciology* 2001; **32**:281–284.
6. Tai Y-C, Noelle S, Gray JMNT, Hutter K. An accurate shock-capturing finite-difference method to solve the Savage–Hutter equations in avalanche dynamics. *Annals of Glaciology* 2001; **32**:263–267.
7. Gray JMNT, Wieland M, Hutter K. Gravity-driven free surface flow of granular avalanches over complex basal topography. *Proceedings of the Royal Society of London*, *Series A* 1999; **455**:1841–1874.
8. Wieland M, Gray JMNT, Hutter K. Channelized free-surface flow of cohesionless granular avalanches in a chute with shallow lateral curvature. *Journal of Fluid Mechanics* 1999; **392**:73–100.
9. Berezin YA, Hutter K, Spodareva LA. Stability properties of shallow granular flows. *International Journal of Nonlinear Mechanics* 1998; **33**(4):647–658.
10. Gray JMNT, Hutter K. Pattern formation in granular avalanches. *Continuum Mechanics and Thermodynamics* 1997; **9**:341–345.
11. Gray JMNT. Granular flow in partially filled slowly rotating drums. *Journal of Fluid Mechanics* 2001; **441**:1–29.
12. Hutter K. Avalanche dynamics. In *Hydrology of Disasters*, Singh VP (ed.). Kluwer Academic Publishers: Dordrecht, 1996; 317–394.
13. Hutter K, Koch T, Plüss C, Savage SB. The dynamics of avalanches of granular materials from initiation to runout. Part II. Experiments. *Acta Mechanica* 1995; **109**:127–165.
14. Hutter K, Rajagopal KR. On flows of granular materials. *Continuum Mechanics and Thermodynamics* 1994; **6**:81–139.
15. Koch T, Greve R, Hutter K. Unconfined flow of granular avalanches along a partly curved surface. II. Experiments and numerical computations. *Proceedings of the Royal Society of London*, *Series A* 1994; **445**:415–435.
16. Greve R, Hutter K. Motion of a granular avalanche in a convex and concave curved chute: experiments and theoretical predictions. *Philosophical Transactions of the Royal Society of London*, *Series A* 1993; **342**:573–600.
17. Hutter K, Siegel M, Savage SB, Nohguchi Y. Two-dimensional spreading of a granular avalanche down an inclined plane. Part I: theory. *Acta Mechanica* 1993; **100**:37–68.
18. Jaeger HM, Nagel SR. Physics of the granular state. *Science* 1992; **255**:1523.
19. Nagel SR. Instabilities in a sandpile. *Review of Modern Physics* 1992; **64**:321.
20. Liu CH, Jaeger HM, Nagel SR. Finite size effects in a sandpile. *Physical Review A* 1991; **43**:7091.
21. Liu CH, Nagel SR. Sound in a granular material: disorder and nonlinearity. *Physical Review B* 1993; **48**:15646.
22. Jaeger HM, Knight JB, Liu CH, Nagel SR. What is shaking in the sand box? *Material Research Society Bulletin* 1994; **19**:25.
23. Jaeger HM, Nagel SR, Behringer RP. The physics of granular materials. *Physics Today* 1996; **4**:32.
24. Jaeger HM, Nagel SR, Behringer RP. Granular solids, liquids and gases. *Reviews of Modern Physics* 1996; **68**:1259.
25. Jaeger HM, Nagel SR. Dynamics of granular materials. *American Scientist* 1997; **85**:540.

DOI: 10.1002/nme

26. Cheng X, Varas G, Citron D, Jaeger HM, Nagel R. Collective behavior in a granular jet: emergence of a liquid with zero surface tension. *Physical Review Letters* 2007; **99**:188001.
27. Zohdi TI. Modeling and direct simulation of near-field granular flow. *The International Journal of Solids and Structures* 2004; **42**(2):539–564.
28. Zohdi TI. A computational framework for agglomeration in thermo-chemically reacting granular flows. *Proceedings of the Royal Society* 2004; **460**:3421–3445.
29. Zohdi TI. Charge-induced clustering in multifield granular flow. *The International Journal of Numerical Methods in Engineering* 2005; **62**:870–898.
30. Zohdi TI. Computation of strongly coupled multifield interaction in particle–fluid systems. *Computer Methods in Applied Mechanics and Engineering* 2007; **196**:3927–3950.
31. Ciampini D, Spelt JK, Papini M. Simulation of interference effects in particle streams following impact with a flat surface. Part I. Theory and analysis. *Wear* 2003; **254**:237–249.
32. Ciampini D, Spelt JK, Papini M. Simulation of interference effects in particle streams following impact with a flat surface. Part II. Parametric study and implications for erosion testing and blast cleaning. *Wear* 2003; **254**:250–264.
33. Gomes-Ferreira C, Ciampini D, Papini M. The effect of inter-particle collisions in erosive streams on the distribution of energy flux incident to a flat surface. *Tribology International* 2004; **37**:791–807.
34. Goldsmith W. *Impact*: *The Theory and Physical Behavior of Colliding Solids*. Dover: Toronto, 2001.
35. Johnson K. *Contact Mechanics*. Cambridge University Press: Cambridge, 1985.
36. Haile JM. *Molecular Dynamics Simulation*: *Elementary Methods*. Wiley: New York, 1992.
37. Pöschel T, Schwager T. *Computational Granular Dynamics*. Springer: Berlin, 2004.
38. Ghobeity A, Spelt JK, Papini M. Abrasive jet micro-machining of planar areas and transitional slopes. *Journal of Micromechanics and Microengineering* 2008; **18**:055014.
39. Ghobeity A, Krajac T, Burzynski T, Papini M, Spelt JK. Surface evolution models in abrasive jet micromachining. *Wear* 2008; **264**:185–198.

DOI: 10.1002/nme